ADVANCED FUNCTIONAL MATERIALS
www.afm-journal.de

Highly Efficient 1D/3D Ferroelectric Perovskite Solar Cell

Haijuan Zhang, Zejiao Shi, Laigui Hu, Yuan-Yuan Tang, Zhengyuan Qin, Wei-Qiang Liao, Zi Shuai Wang, Jiajun Qin, Xiaoguo Li, Haoliang Wang, Meenakshi Gusain, Fengcai Liu, Yiyi Pan, Mingsheng Xu, Jiao Wang, Ran Liu, Chunfeng Zhang, Ren-Gen Xiong, Wei E. I. Sha,* and Yiqiang Zhan**

With the capability to manipulate the built-in field in solar cells, ferroelectricity is found to be a promising attribute for harvesting solar energy in solar cell devices by influencing associated device parameters. Researchers have devoted themselves to the exploration of ferroelectric materials that simultaneously possess strong light absorption and good electric transport properties for a long time. Here, it is presented a novel and facile approach of combining state-of-art light absorption and electric transport properties with ferroelectricity by the incorporation of room temperature 1D ferroelectric perovskite with 3D organic–inorganic hybrid perovskite (OIHP). The 1D/3D mixed OIHP films are found to exhibit evident ferroelectric properties. It is notable that the poling of the 1D/3D mixed ferroelectric OIHP solar cell can increase the average V_{oc} can be increased from 1.13 to 1.16 V, the average PCE from 20.7% to 21.5%. A maximum power conversion efficiency of 22.7%, along with an enhanced fill factor of over 80% and open-circuit voltage of 1.19 V, can be achieved in the champion device. The enhancement is by virtue of reduced surface recombination by ferroelectricity-induced modification of the built-in field. The maximum power point tracking measurement substantiates the retention of ferroelectric-polarization during the continued operation.

1. Introduction

Organic–inorganic hybrid halide perovskites (OIHP) have attracted immense research interest because of their extraordinary optical and electric properties. Since the perovskite has been used as a light absorber in the solar cell in 2009 by Miyasaka et. al,[1] extensive efforts have been made in the direction of exploiting the highly-efficient perovskite solar cells (PSCs),[2–5] attaining the power conversion efficiency (PCE) to 25.2%.[6] The highest achieved short-circuit current (J_{sc}) value for the PSCs is over 25.0 mA cm^{-2}, which is almost close to its theoretical maximum value, defined by the Shockley–Queisser (S–Q) limit.[7] However, there is still a requirement to explore the OIHP for the improvement of open-circuit voltage (V_{oc}) and fill factor (FF).[5,8] Non-radiative recombination process in the PSCs is considered to be the main reason contributing to the energy losses affecting V_{oc} and FF. Intense efforts have been made to reduce the non-radiative recombination, such as interface passivation,[5,9,10] additive engineering,[11–13] and low dimension perovskite mixing,[14–17] in order to improve V_{oc} and FF. Research in this direction leads to the V_{oc} approaching 95% of the S–Q limit and FF over 80%.[5] Further improvement in the PCEs by optimizing OIHP film and device structure is now a major concern.

H. Zhang, Z. Shi, L. Hu, J. Qin, X. Li, H. Wang, Dr. M. Gusain, F. liu, Y. Pan, M. Xu, Dr. J. Wang, Prof. R. Liu, Prof. Y. Zhan
Center for Micro Nano Systems, School of Information Science and Technology (SIST)
Fudan University
Shanghai 200433, P. R. China
E-mail: yqzhan@fudan.edu.cn

Dr. Y.-Y. Tang, Dr. W.-Q. Liao, Prof. R.-G. Xiong
Ordered Matter Science Research Center
Nanchang University
Nanchang 330031, P. R. China
E-mail: xiongrg@seu.edu.cn

Z. Qin, C. Zhang
National Laboratory of Solid State Microstructures, School of Physics, and Collaborative Innovation Center for Advanced Microstructures
Nanjing University
Nanjing 210093, P. R. China

The ORCID identification number(s) for the author(s) of this article can be found under https://doi.org/10.1002/adfm.202100205.

Z. S. Wang
Department of Electrical and Electronic Engineering
The University of Hong Kong
Hong Kong 999077, P. R. China

Prof. R.-G. Xiong
Jiangsu Key Laboratory for Science and Applications of Molecular Ferroelectrics
Southeast University
Nanjing 211189, P. R. China

Prof. W. E. I. Sha
State Key Laboratory of Modern Optical Instrumentation
College of Information Science and Electronic Engineering
Zhejiang University
Hangzhou 310027, P. R. China
E-mail: weisha@zju.edu.cn

DOI: 10.1002/adfm.202100205

Different from p-i-n photovoltaic devices, in which charge separations are heavily determined by the intrinsic properties of light absorption material and the selective contacts in the devices,[18] ferroelectric polarization was found to play a dominant role in the ferroelectric solar cell for charge separation and transport.[19–21] Previously, ferroelectric P–E behavior from tetragonal $MAPbI_3$ single crystals has been confirmed as a result of the dielectric response by various groups.[22,23] The giant switchable photovoltaic effect in the 3D PSCs has also been ascribed to the ferroelectric polarization.[24,25] However, confirming the existence of ferroelectricity in polycrystalline films and its role in device performance enhancement are always vital debating issue,[26–28] in view of the fact that similar switchable voltage can also be induced by ion migration in the 3D OIHP film.[29,30] On the other hand, OIHP ferroelectrics especially low dimensional OIHP ferroelectrics, recently have been successfully exploited by Xiong et. al.[31–36] Unfortunately, the low dimensional OIHPs exhibit large band gaps owing to quantum confinement effect and limited carrier mobility induced by the long chain of organic ligands.[37] Therefore, it is difficult to directly use low-dimensional OIHP ferroelectrics as light absorption materials.[38] In regards to the conventional non-ferroelectric low dimensional OIHP, the aforementioned disadvantages could be alleviated by mixing low dimensional OIHP with conventional 3D OIHP[14–17] as light absorbers.

Here we show that 1D/3D mixed OIHP can be formed by the incorporation of room temperature 1D ferroelectric OIHP$[(CH_3)_3NCH_2I]PbI_3$ (trimethyliodomethylammonium tris(μ_2-iodo)-lead, $TMIMPbI_3$)[32] with 3D OIHP $(FAPbI_3)_{0.85}(MAPbBr_3)_{0.15}$, benefitting from their same PbI_6 octahedra backbone.[39–41] The 1D/3D mixed OIHP films were found to exhibit evident ferroelectric properties. With an optimized ratio of 1D OIHP, in the 1D/3D mixed PSCs, we observed improvement in J_{sc} and FF, increasing the PCE values from 20.2 ± 1.2% to 20.7 ± 1.3%. More interestingly, after poling the device with +1 V under dark condition, the average V_{oc} can be increased from 1.14 ± 0.04 V to 1.16 ± 0.03 V. The highest V_{oc} value for the champion device is 1.19 V, approaching the S–Q limit.[5] After positive poling, an average PCE of 21.5% is achieved, with the PCE of 22.7% in a champion device. After excluding the ion migration effect by a low temperature (ion frozen at 250 K) polarization, the ferroelectric polarization of the 1D/3D mixed OIHP film is proved to be responsible for the performance enhancement. The drift-diffusion simulation results suggest the enhancement is due to the reduced surface recombination by ferroelectricity-induced modification of the built-in field.

2. Results and Discussions

2.1. Properties of 1D/3D Mixed OIHP Films

The 1D/3D mixed OIHP film was fabricated by a standard two-step method.[3,42–44] The $[(CH_3)_3NCH_2I]I$ (TMIMI) are mixed with PbI_2 in the precursor solution, which is first spin-coated on the ITO/SnO_2 substrate. Then formamidinium (FA)/methylammonium (MA) solution is spin-coated on the top of the PbI_2 layer, forming a mixed structure of the 1D/3D OIHP film $(TMIMPbI_3)_x$:$[(FAPbI_3)_{0.85}(MAPbBr_3)_{0.15}]_{1-x}$ after appropriate annealing. In **Figure 1**a,b, the scanning electron microscopy (SEM) images of the 3D OIHP film (control) and 1D/3D mixed OIHP film ($x = 0.6\%$) has been presented showing smooth and pinhole-free surface. Mixing 1D perovskite brings no obvious change in the morphology. The systematic cross-section SEM study of 1D/3D mixed perovskite films has also been carried out and is presented in Figure S1, Supporting Information. The cross-sectional SEM image of 3D perovskite (Figure S1a, Supporting Information) shows a very smooth cross-section surface, with the same grain size as observed from the top-view SEM morphology image as shown in Figure S2, Supporting Information. The thickness of perovskite layer is around 500 nm, estimated from cross-sectional SEM image. After doping with the 1D OIHP phase in 3D OIHP, the wrinkles appear in the cross-section SEM images. With an increase in the ratio of 1D OIHP phase, the wrinkles become prominent and observed clearly in Figure S1b–d, Supporting Information, suggesting the presence of wrinkles probably due to the introduction of 1D phase of OIHP. To further investigate the conjunction of 1D and 3D OIHP phases, high-resolution transmission electron microscope (HRTEM) was performed. From the HRTEM image (Figure 1c), the 1D phase and 3D phase can be identified according to the different lattice constants as marked by yellow and red circles, respectively. The existence of 1D phase in the 1D/3D mixed OIHP film can be evidenced by the X-ray diffraction (XRD) analysis as well (Figure 1d). A strong peak at 12.7° belongs to the unreacted PbI_2, which usually can be observed in the two-step fabrication processed perovskite films.[44] With increasing the molar ratio of TMIMI in the second step precursor solution, the peak corresponding to PbI_2 dramatically decreases. The decrease in the peak intensity of PbI_2 in XRD pattern indicates the formation of $TMIMPbI_3$ resulting from the reaction of PbI_2 with TMIMI. Furthermore, a small peak at $2\theta \approx 10°$ has been clearly observed in the 1D/3D mixed film as shown in the inset of Figure 1d, which can be attributed to the presence of 1D phase ($TMIMPbI_3$) in the 1D/3D mixed film.[32] According to Bragg's law ($2d\sin\theta = n\lambda$), 2θ value of 10.871° can be deduced from the lattice constant (8.138 Å) measured from the yellow highlighted portion in HRTEM image represented in Figure 1c, which perfectly supports the XRD results. And the (220) *hkl* facet of 3D OIHP phase can be also identified in the adjacent area highlighted with red color. With all the aforementioned results, it is confirmed that by adding the 1D perovskite in the precursor, the 1D/3D mixed perovskite film can be formed. The 1D phase is randomly distributed in the film with no obvious phase separation, showing 1D/3D mixed OIHP is an indivisible whole sharing with the same PbI_6 octahedra backbone, similar to the previously reported 1D/3D structure.[45,46] The absorption and photoluminescence (PL) of the 1D/3D mixed OIHP film are shown in Figure 1e. Only a few nanometer blue shift from the absorption and red shift from PL have been observed in the mixed film as compared with that of 3D OIHP film. The time-resolved PL (TRPL) results show similar PL lifetime of control and 1D/3D mixed OIHP film, as presented in Figure S3, Supporting Information.

Piezoresponse force microscopy (PFM), a powerful tool for both probing and switching the local ferroelectric polarization at the microscale, was utilized to characterize the 1D/3D mixed OIHP films. **Figure 2** exhibits the vertical PFM phase and amplitude images in the 1D/3D mixed OIHP film (around 1.1 μm). In the amplitude image of Figure 2b, it is clear that most of the

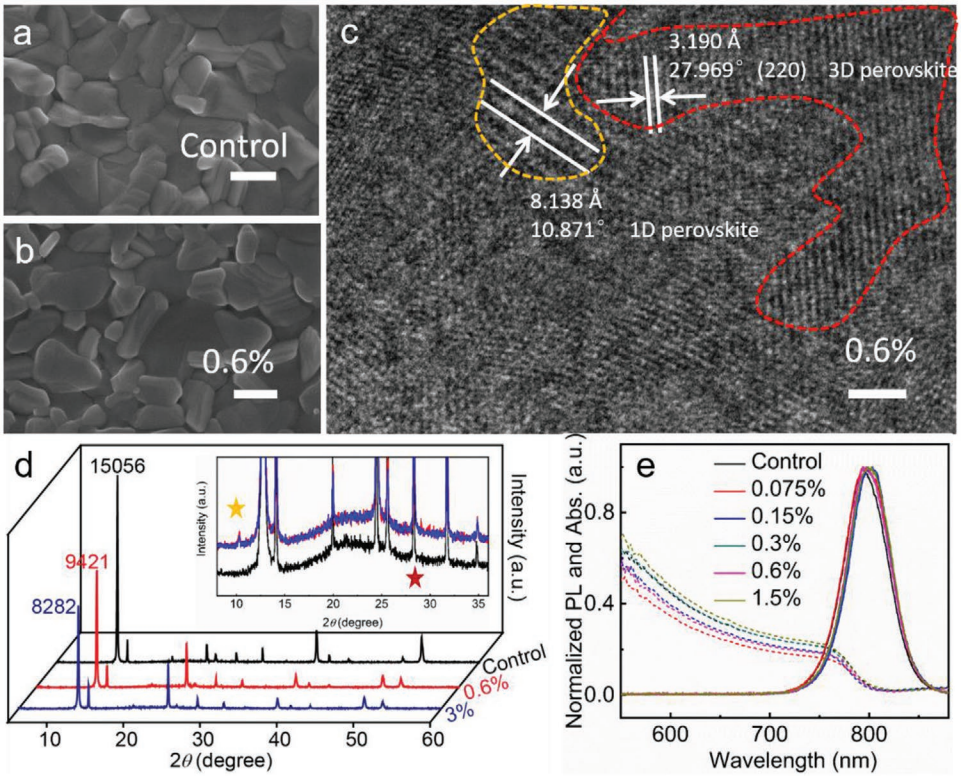

Figure 1. a,b) Top-view SEM images of the control and 0.6% molar ratio 1D/3D mixed OIHP films. Scale bar: 0.2 µm. c) HRTEM image of 0.6% molar ratio 1D/3D mixed perovskite. Scale bar: 2 nm. d) XRD patterns of the control and 1D/3D mixed OIHP films. The diffraction peaks marked in yellow and red color is corresponding to the 1D perovskite phase ($TMIMPbI_3$) and 3D perovskite phase in the 1D/3D mixed OIHP film, respectively. e) PL and UV–vis data for the control and 1D/3D mixed OIHP films.

regions have relatively weak signals, where the phase signals are not uniform and vary greatly (Figure 2a), but a few grains have very strong signals (Figure 2b). Moreover, antiparallel domains can be seen in these grains, where the phase image presents a clear 180° contrast with yellow and purple colors and dark features in the amplitude contrast indicate the presence of domain walls (Figure 2a,b). By overlaying the PFM mappings on a 3D topography (Figure S4, Supporting Information), we can see that the piezoresponse has no obvious correlation with the sample topography. These results suggested the coexistence of 1D and 3D phase in 1D/3D mixed OIHP film. Subsequently, we chose a point indicated by blue point marked in Figure 2a to perform the local PFM-based hysteresis loop measurement and presented it in Figure 2d and Figure S5, Supporting Information. The characteristic hysteresis and butterfly loop triggered by the applied direct current (DC) bias is a typical demonstration for the polarization switching of ferroelectric domains. During the polarization switching processes, the surface topography of the thin film (1D/3D mixed OIHP) shows no change (Figure S6, Supporting Information). All the above evidence unambiguously establishes the presence of ferroelectricity in the 1D/3D mixed OIHP films.

2.2. Performance of the 1D/3D Mixed OIHP Ferroelectric Solar Cell

Later, we fabricate 1D/3D mixed PSCs (denoted as "mixed device"), with a device structure of ITO/SnO_2/(1D/3D mixed OIHP)/Spiro-OMeTAD/Au. In the meantime, a control device was also fabricated, with a standard structure of ITO/SnO_2/3D OIHP/Spiro-OMeTAD/Au. The photovoltaic performance of the control and mixed PSCs based on 3D OIHP and 1D/3D mixed ferroelectric OIHP respectively were investigated. **Figure 3**a gives the *J*–*V* curves of the control and optimized mixed PSCs, showing J_{sc} of 24.0 and 24.2 mA cm^{-2}, V_{oc} of 1.13 and 1.15 V, and FF of 76% and 75%, resulting in a PCE of 20.5% and 21.0% respectively. The curve of Figure 3b shows the corresponding external quantum efficiency (EQE) and the integrated photocurrent of the control and mixed PSCs. The measured J_{sc} values are consistent with the integrated J_{sc} of 23.0 (control) and 23.4 (mixed) mA cm^{-2}, determined from EQE. The hysteresis can be also greatly reduced for the 1D/3D mixed ferroelectric PSCs, as shown in Figure S7, Supporting Information and listed in Table S1, Supporting Information.

The detailed parameters are shown in Figure 3c–f and summarized in **Table 1**, includes the average and optimum (from different devices) values of J_{sc} and V_{oc}, FF and PCE. As compared to the control device, the average value of J_{sc} and FF increase from 23.3 mA cm^{-2} and 76% to 23.5% mA cm^{-2} and 77% in the mixed device with the 1D perovskite phase concentration of 0.6%. This indicates that the presence of 1D phase perovskite could efficiently passivate the defects as other low dimensional perovskites.[15–17] With the unchanged V_{oc}, the PCE increased from 20.2% (control) to 20.7% (mixed). The detailed optimization results of the 1D OIHP molar ratio are shown in

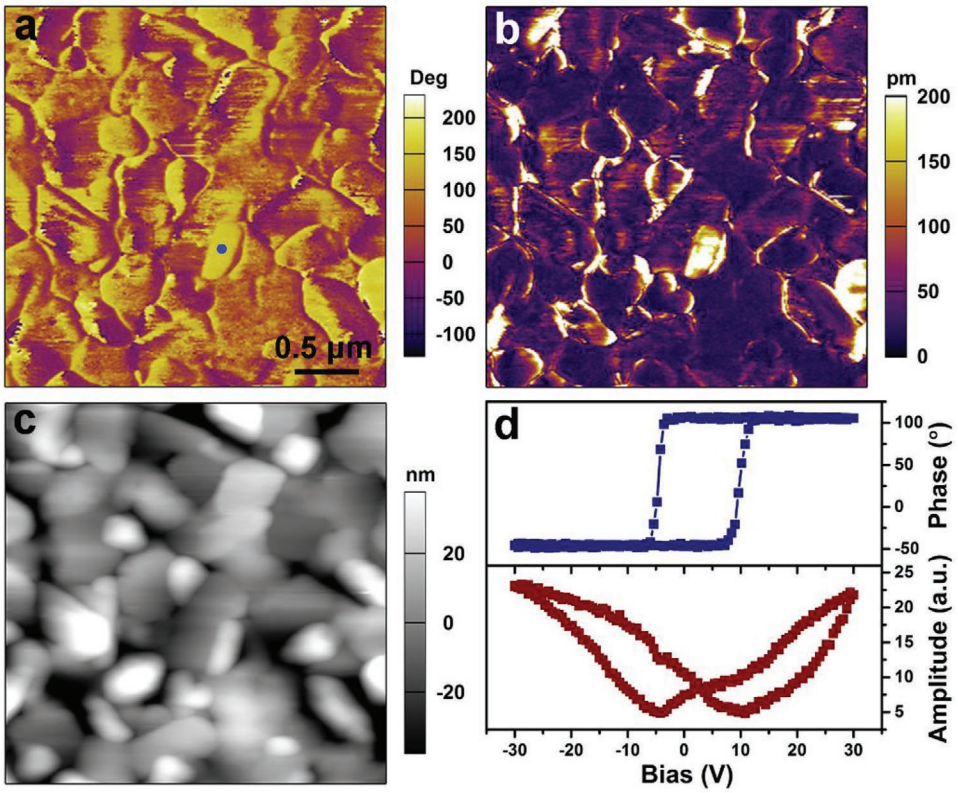

Figure 2. PFM phase (a) and amplitude images (b), and topographic image (c) of the thin film (1D/3D mixed OIHP). d) Dependence of phase and amplitude signals with applied DC bias for a selected point indicated by blue point marked in Figure 2a, showing a hysteresis loop and a butterfly curve.

Figure S8, Supporting Information. With increasing the concentration of 1D OIHP to 0.6%, both the J_{sc} and FF increase, while the V_{oc} shows no remarkable change. However, further increase in the concentration of 1D OIHP results in the reduction of the values of J_{sc} and FF and V_{oc}, due to the additional serial resistance brought by 1D OIHP.

Then we pole the mixed device with ±1 V under a dark condition for 5 s, and re-characterized the devices. The poled *J–V* curves are also shown in Figure 3a, a clear increase of V_{oc} (from 1.15 to 1.18 V) and FF (from 75% to 79%) can be observed in the positively poled mixed device as tabulated in Table S2, Supporting Information, resulting in a substantial improvement in the PCE from 21.0% to 22.6% with an unchanged value of J_{sc}. While a negative poling decreases the V_{oc} (1.10 V) and FF (72%), resulting in the reduction of the PCE value to 19.1%. The V_{oc} can be increased to as high as 1.19 V after positive poling as shown in Table 1 and Figure S11, Supporting Information, which is one of the highest V_{oc} among the reported values in the devices with similar structure and fabrication method. We also applied alternative positive and negative poling on the mixed device. The IV curve can be repeatedly performed, as shown in Figures S10 and S11, Supporting Information. To rule out the possible effect of space charge and ion migration, the same treatment is applied to the control device. In spite of the fact, that the positive or negative poling is applied, in Figure 3a the *J–V* curve of the control device remains almost the same. Sometimes the PCE of the control device even slightly decreases as shown in Figure S12, Supporting Information. Therefore, we can conclude that the ferroelectricity of the 1D/3D mixed OIHP film has to be responsible for the performance enhancement. The performance parameters of the control and optimized mixed devices after positive poling are shown as the statistical charts in Figure 3c–f, while the poling effect of all the devices with different concentrations of 1D OIHP phase is also shown in Figure S9a–d, Supporting Information. The average J_{sc} almost remains unchanged in all the devices, while the V_{oc} and FF start to appear an obvious increase when the concentration of mixed 1D phase perovskite is over 0.3%. For the optimized 0.6% device, the average FF increases from 77% to 78%, the V_{oc} increases from 1.14 to 1.16 V after positive poling. Taking all the parameters into account, an average PCE of 21.6% has been achieved in the optimized positively-poled device. The maximum J_{sc}, V_{oc}, FF, and PCE of the positively-poled device are 24.5 mA cm^{-2}, 1.19 V, 80%, and 22.7%, respectively. Although the performance became worse with further increasing the concentration of 1D OIHP to 1.5%, the maximum enhancement has been achieved by poling these devices. The average V_{oc} increased from 1.10 to 1.15 V, the average PCE increased from 19.5% to 21.2%.

To confirm the retention of the ferroelectric polarization, the V_{oc} of the PSCs before poling and after positive/negative poling stored in glovebox has been monitored separately for more than 116.7 h, as displayed in **Figure 4**a. The three V_{oc} values keep almost constant during the whole time, showing no observable depolarization. Likewise, the long-term stability of the control and the positively poled 1D/3D mixed PSCs in

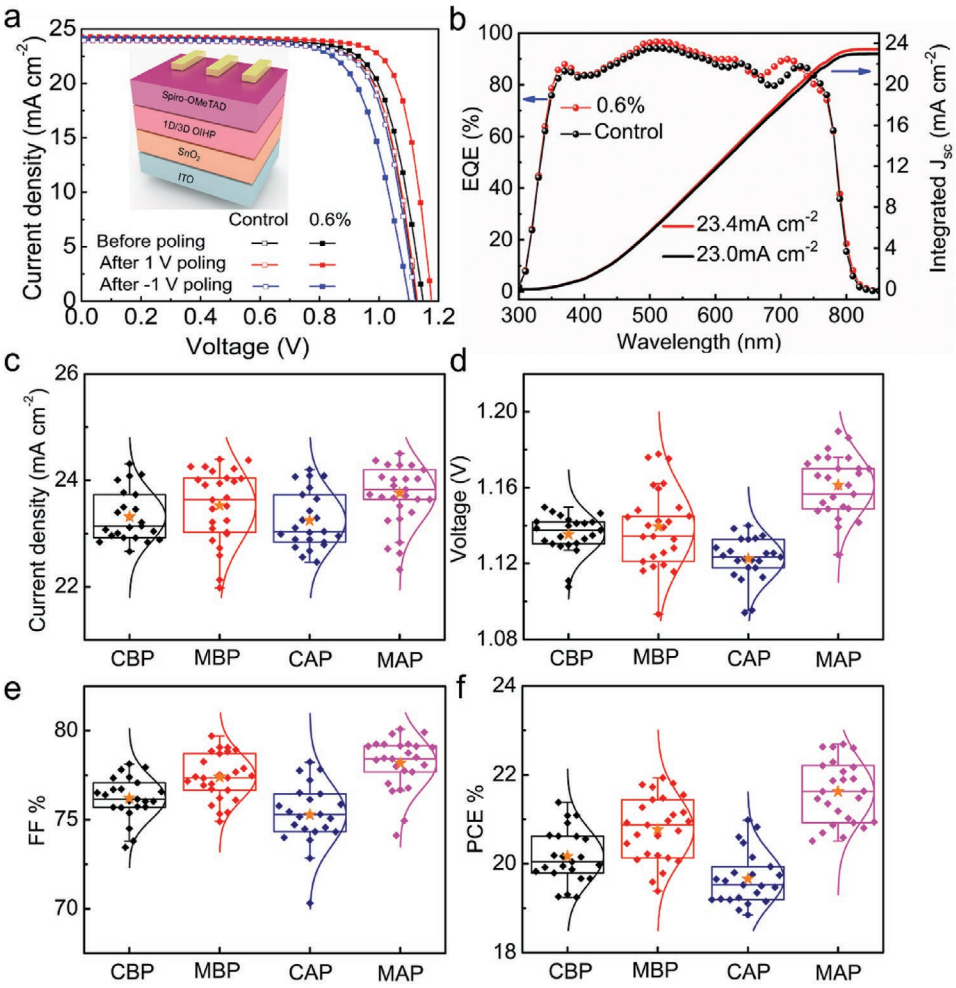

Figure 3. a) *J–V* curves of control and 1D/3D mixed PSCs before and after poling. b) EQE of control and 1D/3D mixed PSCs. The integrated J_{sc} from the EQE is 23.0 and 23.4 mA cm^{-2}, respectively. c–f) Statistics of J_{sc}, V_{oc}, FF(%), and PCE(%) parameters of control and 1D/3D mixed PSCs before and after poling. CBP, MBP, CAP, and MAP represent control before poling, mixed before poling, control after poling, and mixed after poling, respectively.

ambient environment (50% humidity) were also studied and the results are shown in Figure 4b. In high humidity ambient environment, the value of PCE of 1D/3D mixed PSCs decreases to less than 5% over 116.7 h, while control devices PCEs decline up to 25%. We also measured PCE at maximum power point (MPP) as a function of time for the same cells under different polarization states using MPP tracking method, presented in Figure 4c,d. As mentioned, the PCE of control PSCs decreases after positive or negative poling as shown in Figure S12, Supporting Information. The PCE of the control PSC at MPPs under positive and negative polarization gradually recovers to the original value before poling in first 50 s and overlap with each other after that, suggesting the probability of ion migration under an external electric field which results in the reduction of performance of the control device after poling. During the continued operation, the ions diffuse back to original position, resulting in the recovery of the PCE. The overlapping MPP curves after 50 s indicate that the ion migration cannot provide a stabilized polarization. The PCE at MPPs of the mixed PSC under positive and negative polarization is

Table 1. Statistics of J_{sc}, V_{oc}, FF, and PCE parameters of control and 1D/3D mixed PSCs before and after poling.

Devices	J_{sc} [mA cm^{-2}]		V_{oc} [V]		FF [%]		PCE [%]	
	Average	Champion	Average	Champion	Average	Champion	Average	Champion
CBP	23.3	23.9	1.14	1.15	76	78	20.2	21.3
CAP	23.2	24.1	1.12	1.12	75	78	19.7	21.0
MBP	23.5	24.4	1.14	1.14	77	79	20.8	21.9
MAP	23.7	24.5	1.16	1.17	78	79	21.6	22.7

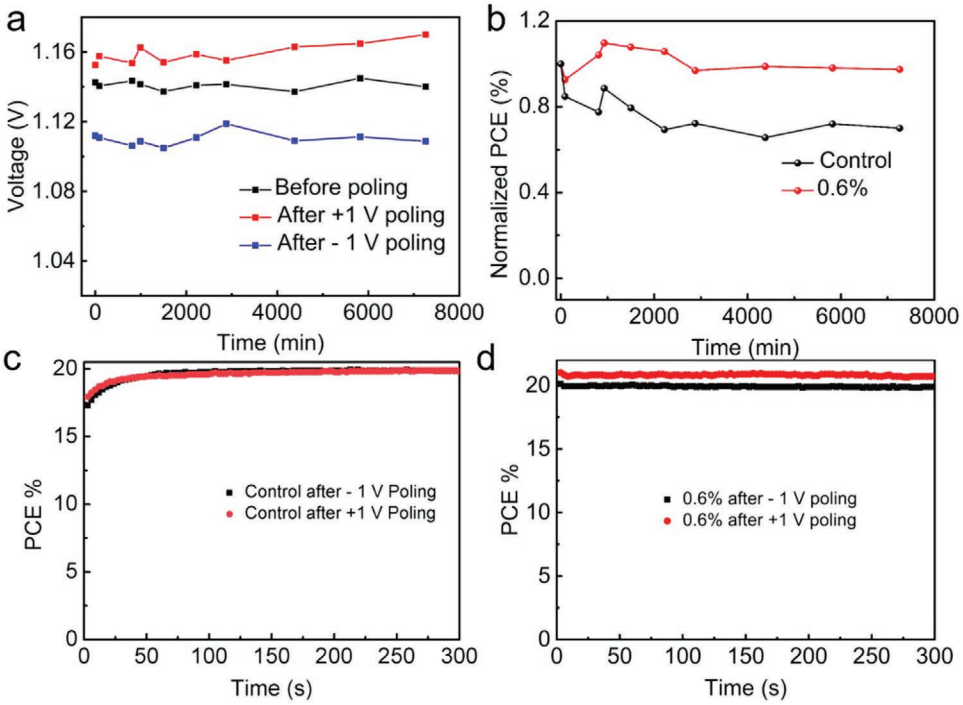

Figure 4. a) V_{oc} stability of 1D/3D mixed PSCs before and after poling. b) PCE stability of control and 1D/3D mixed PSCs after positively poling. c) Stable power output of the MPP of the control device before and after poling. d) Stable power output of the MPP of the 1D/3D mixed PSCs before and after poling.

also measured, shown in Figure 4d. The PCE at the MPP of the mixed PSC under positive polarization is higher than that under negative polarization at the beginning. Contrary to the control PSC, the margin of PCE in the mixed PSC is kept for the whole continued operation, confirming a stabilized polarization is installed in the mixed PSC. The well-retained polarization cannot be induced by the ion migration, therefore must be attributed to ferroelectricity of the 1D/3D mixed OIHP.

To further examine the origin of the improved device characteristics, we also fabricate PSCs with a 1D/3D mixed OIHP capping structure as shown in Figure S13, Supporting Information, made by spin coating of TMIMI solution on $(FAPbI_3)_{0.85}(MAPbBr_3)_{0.15}$ films prepared by standard two-step method at the third step. As shown in Figure S14, Supporting Information, the devices with 1D/3D mixed OIHP capping structure has better J_{sc} and FF, similar to results of other low-dimension perovskite capping structure.[17,47–48] However, the poor conductivity of $TMIMPbI_3$ brings in additional serial resistance, thus reducing the V_{oc}. After positively poling the device, similar V_{oc} enhancement has also been observed in the capping device (Figure S15, Supporting Information), supporting our result that the universal enhancement is ascribed to the induced polarization in the 1D/3D mixed OIHP capping layer.

As shown in Figure S17, Supporting Information, the measurement results of high-frequency capacitances (>10 kHz) of the ferroelectric 1D/3D mixed OIHP are fitted by the Debye model. The static or low-frequency capacitance (<1 kHz) is extrapolated by the Debye model to eliminate the influences of carrier transport and ion migration. Compared to the control device, the static capacitance of the mixed OIHP increased by four times after poling, which contributes to the ferroelectric effect. It is already known that the extrapolated static capacitance equals the geometric capacitance expressed as:

$$C_{geo} = \frac{\varepsilon_0 \varepsilon_r A}{d} \quad (1)$$

where A is the area of the device, d is the thickness, and ε_0, ε_r are the vacuum and relative dielectric constants. Since these devices are of the same thickness and area, measured in the same situation, the increasing capacitances indicate the significant increase of the dielectric constant of the mixed OIHP after poling induced by the ferroelectric effect. Based on the above understanding and argument, theoretical analyses have been conducted through 1D drift-diffusion simulation, which qualitatively proves the enhanced V_{oc} of the 1D/3D OIHP ferroelectric PSC after positive poling. The details of the drift-diffusion simulation tool and the parameters used can be seen in Supporting Information.

According to capacitance experiments, we assume that ε_r is increased by four times in the OIHP of the ferroelectric modeling device, after positive poling, and the rest of the input parameters were completely the same. The effect of the enlarged ε_r on the electric potential and electric field can be seen in **Figure 5**a,b. Particularly, the boost of ε_r would result in the reduced electric potential drop in the OIHP layer and therefore larger electric-field at the interfaces between OIHP and carrier transporting layers (CTLs).

The effects of the large electric field were explored in the simulation of the J–V curves of PSCs. Through comparing

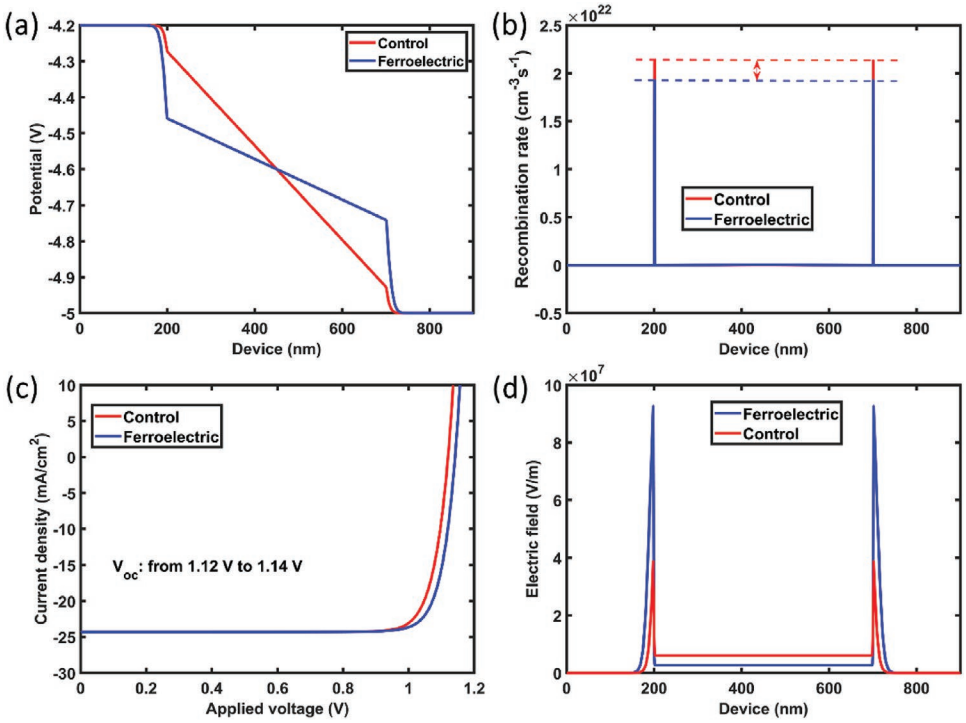

Figure 5. Compare the simulated electric potentials (a) and electric fields (b) in the ferroelectric PSC before and after positive poling at short-circuit state. c) Compare the simulated *J–V* curves of the ferroelectric PSC before and after positive poling with the large density of the recombination center at the interface. d) Compare the simulated recombination rate profiles in the ferroelectric PSC before and after positive poling at MPP.

simulated *J–V* curves of ferroelectric PSC before and after positive poling (Figure 5c), V_{oc} increase from 1.12 to 1.14 V. This trend matches well with our experimental results. In these modeling devices, the density of trap-assisted Shockley–Read–Hall (SRH) recombination center in the OIHP bulk was set to be weaker than that at the interface between OIHP and CTLs, which satisfied the consensus of high-performance PSCs that the main loss occurs at the interface but not in the bulk. The improvements of V_{oc} can be explained as the much stronger electric field at the interfaces will facilitate the carrier collection across the interfacial region, and therefore decrease the carrier loss caused by the interfacial recombination. The carrier generated in the absorber will be quickly extracted to the electrodes before they recombine with each other at the interface. The SRH recombination rate profiles of the ferroelectric PSC before and after positive poling at the MPP state were compared and presented in Figure 5d. The recombination at the interfaces is dominant in the ferroelectric PSC before and after positive poling, while the recombination rate in the ferroelectric PSC before poling is higher than that after positive poling, which is consistent with our explanation. On the contrary, if the recombination at the interfaces is negligible compared to that in the bulk (Figure S18), we should observe the improvement of FF, but the improvement in V_{oc} is ignorable, which is not supporting our experimental results. Therefore, from simulation, we can conclude that the efficiency improvement of ferroelectric PSCs should be attributed to the suppression of interfacial recombination, which originates from the stronger electric field at the interface, as the result of ferroelectric polarization. Further proof for subdued traps-assisted recombination is acquired from light intensity dependent V_{oc} plots in Figure S19, Supporting Information. Not only the higher V_{oc} at every individual light intensity but also the lower slope suggests restrained voltage loss for positively polarized ferroelectric PSCs from SRH recombination, which is in good agreement with the simulation results.

However, one concern regarding our explanations is about ion migration, as the accumulation of the mobile ion at the interfaces between OIHP and CTLs will also enlarge the electric field, and then increase V_{oc}. In order to exclude the effect of ion migration from our discussion, we measured the dark current of control and ferroelectric PSCs with and without poling at the low temperature (250 K), in which condition the hopping of mobile ion will be almost negligible.[49] The result in Figure S20, Supporting Information, shows that there is no observable change of the *J–V* curves in control device after positive or negative polarization at 250 K. However, in ferroelectric PSCs even without ion migration, the current before and after poling will still differ much. Considering ion migration which occurs in regular 3D perovskites could be suppressed by adding low dimensional perovskite, the huge difference of *J–V* curves indicates polarization field is contributed by ferroelectric property of 1D/3D mixed OIHP. The different shifts of *J–V* curves also prove that the electric field arising from ferroelectric polarization is much higher than that of mobile ions (see Supporting Information).

Additionally, a fundamental question lies at whether the ferroelectric effect could help PSCs to approach their S–Q limit.[50,51] If ignorable bulk recombination (surface recombination still exists) and sufficiently high mobility are assumed

for the active materials, Figure S21, Supporting Information, shows that an extremely large dielectric constant surprisingly makes ferroelectric PSCs approaching the S–Q limit.

Though organic ferroelectric material P(VDF-TrFE) has very recently been used in PSCs[52,53] to enhance conversion efficiency, undisputed evidence for the ferroelectricity which was proposed for the reason of efficiency enhancement is still lacking, such as strong piezoelectric response, the repeatable and nonvolatile poling-induced performance enhancement, and especially, perfect hysteresis loops with the 180° domain walls, by considering that nonferroelectric materials may also exhibit PFM signals and poling effect due to the space charge effect. Our study clearly demonstrates that the ferroelectricity of the 1D/3D hybrid perovskite is responsible for its high conversion efficiency by providing the phase and amplitude loops with the 180° domain walls. Moreover, because of the intrinsic difference between polymer and OIHP, the morphology of the OIHP film is strongly affected[53] by increasing the concentration of ferroelectric polymer, resulting in an influenced device performance. In contrast, 1D ferroelectric perovskite $TMIMPbI_3$ possesses the same PbI_6 octahedra backbone as 3D OIHP, which allows the formation of 1D/3D hybrid perovskite as an indivisible whole. Considering that the dielectric constant of the 3D OIHP (ε_{3D} = 47) is much larger than that of 1D OIHP (ε_{3D} = 13), the large relaxational dipoles in the 3D OIHP could stabilize the ferroelectric polarization of the 1D OIHP, identical to the role of the amorphous phase in pure P(VDF-TrFE) ferroelectric films.[54] Therefore, the 1D phase can make the whole 1D/3D hybrid grains exhibit ferroelectric properties. In addition, the morphology of 1D/3D hybrid perovskite films shows almost no influence with increasing the concentration of 1D phase, as shown in Figure S2, Supporting Information, ensuring a state-of-art performance from 1D/3D hybrid PSC.

3. Conclusions

In summary, we have successfully demonstrated the ferroelectricity of the 1D/3D mixed OIHP which can be favorable for highly-efficient PSCs. By incorporating 1D ferroelectric perovskite with conventional 3D perovskite, 1D/3D mixed OIHP can be obtained. Ferroelectricity for the mixed OIHP was unambiguously confirmed. The remnant polarization of 1D/3D mixed OIHP, can modulate the V_{oc} and FF of the device by poling. With increasing the FF to over 80% and V_{oc} to 1.19 V, a maximum PCE of 22.7% has been achieved, which is higher than the ferroelectric[55] or ferroelectric-assisted solar cells[52,53] reported to date. The MPP tracking measurement proves the ferroelectric-polarization can be well retained during the continued operation. Finally, a drift-diffusion simulation is introduced and unveils that the efficiency improvement of ferroelectric PSCs after positive poling should be attributed to the suppression of interfacial recombination, which originates from the stronger electric field at the interface, as the result of ferroelectric polarization. By employing low dimensional ferroelectric perovskites with even stronger remnant polarization into this simple mixed structure, a higher FF and V_{oc} can be expected. This easy-to-implement approach paves a new way to fabricate highly efficient ferroelectric PSCs, which theoretically could provide V_{oc} approaching the S–Q limit.

4. Experiment Section

Materials: SnO_2 nanoparticle colloid (tin (IV) oxide, 15% in H_2O) was purchased from Alfa Aesar. N,N-dimethylformamide (DMF), dimethyl sulfoxide (DMSO), 4-tert-butylpyridine (4-TBP), bis (trifluoromethylsulfonyl)-imide lithium salt (Li-TFSI) and Tris(2-(1Hpyrazol-1-yl)-4-tert-butylpyridine) cobalt(III) tri[bis(trifluoromethane) sulfonimide] (FK 209; Co(III) TFSI salt) were purchased from Sigma-Aldrich. Formamidinium iodide (FAI) and methylammonium bromide (MABr) were purchased from Dyesol. Methylammonium chloride (MACl) was purchased from Xi'an Polymer Light Technology Corp. Chlorobenzene, isopropanol (IPA) and acetonitrile (ACN) was purchased from Thermo Fisher. Diiodomethane (98%) and trimethylamine (30 wt% water) were purchased from Aladdin. Diethyl ether was purchased from Sinopharm chemical Reagent Co., Ltd., respectively.

Iodomethylammonium iodide (TMIMI) was synthesized by a reaction of Diiodomethane in ethanol with equal molar amount of trimethylamine (30 wt% water), stirred at room temperature for 10 h. After standing, anhydrous Diethyl ether was slowly dripped into the solution. After TMIMI crystals were precipitated, they were filtered by Brinell funnel. TMIMI crystals were recrystallized three times, and then TMIMI crystals were put into a vacuum oven at 60 °C. Pure TMIMI crystals were obtained 12 h later.

Device Fabrication: ITO-glass was cleaned using surfactant, deionized (DI) water, acetone, isopropanol (IPA), and DI water with ultrasonication for 15 min sequentially and dried with N_2 flow. Before casting, ITO-glass was further cleaned by O_2-plasma treatment for 15 min. Diluted SnO_2 dispersion (1.96% in H_2O) was then deposited on the ITO at 3000 rpm for 30 s followed by annealing in a vacuum oven at 120 °C for 45 min. After that, two-step method was applied to fabricate perovskite layer. For 1D/3D mixed device, PbI_2 (635 mg mL^{-1} in DMF/DMSO (9:1 vol) mixing with different TMIMI molar ratio of 0.075%, 0.15%, 0.30%, 0.45%, 0.6%, and 1.5%) was sequentially first spin-coated on the ITO/SnO_2 substrate at 1600 rpm for 30 s and annealed at 75 °C for 45 s. Waiting for the coated substrate to cool down to room temperature, FA/MA solution (60 mg FAI/9 mg MABr/8 mg MACl in 1 mL IPA) spin-coated on the top of the PbI_2 layer at 2200 rpm for 30 s followed by ambient annealing at 150 °C for 18 min with constant relative humidity of 39% (± 3%) and room temperature of 24 °C (±2 °C). 2,2′,7,7′-tetrakis(N,N-dip-methoxyphenylamine)-9,9′-spirobifluorene (Spiro-OMeTAD) was selected as hole transport layer. Spiro-OMeTAD solution (72.3 mg mL^{-1} Spiro-OMeTAD in chlorobenzene containing with 18 µl Li-TFSI salt (104 mg in 200 ul ACN), 27 µL Co-TFSI salt (60 mg in 200 ul ACN), and 30 µL 4-TBP) was coated on the perovskite film at 3000 rpm for 30 s without any further treatment.

For 1D/3D mixed OIHP capping device, OIHP layer was prepared as the same two-step method without the TMIMI incorporation. After ambient annealing for perovskite, TMIMI (0.2, 0.25, 0.3, 0.5, and 1 mg mL^{-1} in IPA) layer was set on top of perovskite at 3000 rpm for 30 s followed by annealing at 100 °C for 5 min. Finally, 85 nm Au was deposited as counter electrode at 10^{-5} Pa by thermal evaporator. The active area of 0.17 cm^2 on device was defined by a patterned shadow mask during Au deposition.

Material Characterization: The XRD dates were collected by RIGAKU D/MAX-3A diffractometer. The top-view SEM image of perovskite and SnO_2 films were investigated by Hitachi S-4800. HRTEM was collected by Hitachi HT7700 Exalens with acceleration voltage of 200 KV. The transmission spectra and absorption spectra were both measured using F20-UV thin-film analyzer (FILMETRICS) at wavelength range between 300 and 800 nm. The steady-state PL (excitation at 514 nm) and TRPL (excitation at 405 nm and emission at 760 nm) spectra measurements were conducted by a Hitachi F-4600 spectrofluorometer (Japan) and FLS980, Edinburgh Instruments Ltd, respective.

The PFM measurement was carried out on a commercial PFM (Oxford instrument, MFP-3D) with high-voltage package and in-situ heating stage. PFM was based on atomic force microscopy (AFM), with an AC

drive voltage applied to the conductive tip. Conductive Pt/Ir-coated silicon probes (EFM, Nanoworld) were used for domain imaging and polarization switching studies, with a nominal spring constant of ≈2.8 nN nm^{-1} and a free-air resonance frequency of ≈75 kHz. Since the amplitude of the low-frequency vertical PFM was within the noise level of the quadrant photodetector of the AFM, the PFM experiments were performed at contact resonance. The typical drive frequency was in the range of 320 to 380 kHz, depending on the contact resonant frequency.

Device Characterization: The *J–V* curves of the PSCs were measured using a Keithley 2602B source in the N_2 filled glove box at room temperature under AM 1.5 G condition at an intensity of 100 mW cm^{-2}, calibrated by a standard Si solar cell (PVM937, Newport). The light source was a 450 watt xenon lamp (Oriel solar simulator, 94023A). The active area of PSCs is 0.17 cm^2, defined by the cross of patterned Au and ITO electrode, and further calibrated by the microscope. The *J–V* curves were tested both at forward scan (from −0.2 to 1.2 V, step 0.04 V) and reverse scan (from 1.2 to −0.2 V, step 0.04 V) without any pre-conditioning before the test. The sweeping time for each point is 0.05 s, with 0 s interval time. The device poling was done under dark conditions. 1 or −1 V was applied to the device for at least 5 s, poling the device to positive or negative polarization separately. The stability comparison was done by one device. The device was firstly measured without any poling, then measured after positively poling, and finally measured after negatively poling.

The C-F dates of the perovskite devices were measured using a Keysight Technologies B1500 source in the N_2 filled glove box at room temperature. A layer of 1D and 3D mixed perovskite film was deposited on the aluminum splitter finger electrode. The channel width of the split-finger electrode is 10 µm. The capacitance of 1D/3D mixed perovskite device before poling was measured under dark condition, under different frequency. And then the 1D/3D mixed perovskite device was polarized for 70 s at 18 V, which gives similar electric field as on the vertical device. The capacitance of the polarized 1D/3D mixed perovskite device was measured under the same condition. For the comparison, a control device with 3D perovskite and same structure are fabricated and measured.

Supporting Information

Supporting Information is available from the Wiley Online Library or from the author.

Acknowledgements

H.Z., Z.S., and L.H. contributed equally to this work. This work is supported by the National Natural Science Foundation of China (grant numbers 61774046). Natural Science Foundation of Shanghai (No. 20ZR1404000).

Conflict of Interest

The authors declare no conflict of interest.

Data Availability Statement

Research data are not shared.

Keywords

ferroelectric, perovskite solar cells, Shockley–Queisser

Received: February 5, 2021
Revised: March 22, 2021
Published online:

[1] A. Kojima, K. Teshima, Y. Shirai, T. Miyasaka, *J. Am. Chem. Soc.* **2009**, *131*, 6050.
[2] M. M. Lee, J. Teuscher, T. Miyasaka, T. N. Murakami, H. J. Snaith, *Science* **2012**, *338*, 643.
[3] J. H. Im, I. H. Jang, N. Pellet, M. Gr?Tzel, N. G. Park, *Nat. Nanotechnol.* **2014**, *9*, 927.
[4] W. S. Yang, B. W. Park, E. H. Jung, N. J. Jeon, Y. C. Kim, D. U. Lee, S. S. Shin, J. Seo, E. K. Kim, J. H. Noh, *Science* **2017**, *356*, 1376.
[5] Q. Jiang, Y. Zhao, X. Zhang, X. Yang, Y. Chen, Z. Chu, Q. Ye, X. Li, Z. Yin, J. You, *Nat. Photonics* **2019**, *13*, 460.
[6] M. A. Green, E. D. Dunlop, D. H. Levi, J. Hohl-Ebinger, M. Yoshita, A. W. Ho-Baillie, *Prog. Photovoltaics* **2020**, *28*, 3.
[7] W. Shockley, H. J. Queisser, *J. Appl. Phys.* **1961**, *32*, 510.
[8] M. Stolterfoht, C. M. Wolff, Y. Amir, A. Paulke, L. Perdigón-Toro, P. Caprioglio, D. Neher, *Energy Environ. Sci.* **2017**, *10*, 1530.
[9] P. Wang, J. Wang, X. Zhang, H. Wang, X. Cui, S. Yuan, H. Lu, L. Tu, Y. Zhan, L. Zheng, *J. Mater. Chem. A* **2018**, *6*, 15853.
[10] H. Tan, A. Jain, O. Voznyy, X. Lan, F. P. G. De Arquer, J. Z. Fan, R. Quintero-Bermudez, M. Yuan, B. Zhang, Y. Zhao, *Science* **2017**, *355*, 722.
[11] X. Li, M. I. Dar, C. Yi, J. Luo, M. Tschumi, S. M. Zakeeruddin, M. K. Nazeeruddin, H. Han, M. Grätzel, *Nat. Chem.* **2015**, *7*, 703.
[12] C. Qin, T. Matsushima, T. Fujihara, C. Adachi, *Adv. Mater.* **2017**, *29*, 1603808.
[13] X. Zhang, S. Yuan, H. Lu, H. Zhang, P. Wang, X. Cui, Y. Zhang, Q. Liu, J. Wang, Y. Zhan, *ACS Appl. Mater. Interfaces* **2017**, *9*, 36810.
[14] D. H. Cao, C. C. Stoumpos, O. K. Farha, J. T. Hupp, M. G. Kanatzidis, *J. Am. Chem. Soc.* **2015**, *137*, 7843.
[15] Z. Wang, Q. Lin, F. P. Chmiel, N. Sakai, H. J. Snaith, *Nat. Energy* **2017**, *2*, 17135.
[16] S. Gharibzadeh, B. A. Nejand, M. Jakoby, T. Abzieher, D. Hauschild, S. Moghadamzadeh, J. A. Schwenzer, P. Brenner, R. Schmager, A. A. Haghighirad, *Adv. Energy Mater.* **2019**, *9*, 1803699.
[17] Y. Liu, S. Akin, L. Pan, R. Uchida, M. Grtzel, *Sci. Adv.* **2019**, *5*, eaaw2543.
[18] U. Wurfel, A. Cuevas, P. Wurfel, *IEEE J. Photovolt.* **2014**, *5*, 461.
[19] T. Choi, S. Lee, Y. J. Choi, V. Kiryukhin, S.-W. Cheongt, *Science* **2009**, *324*, 63.
[20] S. Y. Yang, J. Seidel, S. J. Byrnes, P. Shafer, C. H. Yang, M. D. Rossell, P. Yu, Y. H. Chu, J. F. Scott, J. W. Ager, *Nat. Nanotechnol.* **2010**, *5*, 143.
[21] P. Lopez-Varo, L. Bertoluzzi, J. Bisquert, M. Alexe, Y. Yuan, *Phys. Rep.* **2016**, *653*, 1.
[22] Y. Rakita, O. Bar-Elli, E. Meirzadeh, H. Kaslasi, Y. Peleg, G. Hodes, I. Lubomirsky, D. Oron, D. Ehre, D. Cahen, *Proc. Natl. Acad. Sci. U. S. A.* **2017**, *114*, E5504.
[23] Q. Dong, J. Song, Y. Fang, Y. Shao, S. Ducharme, J. Huang, *Adv. Mater.* **2016**, *28*, 2816.
[24] B. Chen, J. Shi, X. Zheng, Y. Zhou, K. Zhu, S. Priya, *J. Mater. Chem. A* **2015**, *3*, 7699.
[25] B. Chen, X. Zheng, M. Yang, Y. Zhou, S. Kundu, J. Shi, K. Zhu, S. Priya, *Nano Energy* **2015**, *13*, 582.
[26] Z. Fan, J. Xiao, K. Sun, L. Chen, Y. Hu, J. Ouyang, K. P. Ong, K. Zeng, J. Wang, *J. Phys. Chem. Lett.* **2015**, *6*, 1155.
[27] D. A. Egger, A. Bera, D. Cahen, G. Hodes, T. Kirchartz, L. Kronik, R. Lovrincic, A. M. Rappe, D. R. Reichman, O. Yaffe, *Adv. Mater.* **2018**, *30*, 1800691.
[28] A. Gomez, Q. Wang, A. R. Goni, M. Campoy-Quiles, A. Abate, *Energy Environ. Sci.* **2019**, *12*, 2537.
[29] Z. Xiao, Y. Yuan, Y. Shao, Q. Wang, Q. Dong, C. Bi, P. Sharma, A. Gruverman, J. Huang, *Nat. Mater.* **2015**, *14*, 193.
[30] W. Aron, S. D. Stranks, *ACS Energy Lett.* **2018**, *3*, 1983.
[31] Y. M. You, W. Q. Liao, D. Zhao, H. Y. Ye, Y. Zhang, Q. Zhou, X. Niu, J. Wang, P. F. Li, D. W. Fu, *Science* **2017**, *357*, 306.
[32] X. N. Hua, W. Q. Liao, Y. Y. Tang, P. F. Li, P. P. Shi, D. Zhao, R. G. Xiong, *J. Am. Chem. Soc.* **2018**, *140*, 12296.

[33] X. G. Yong, P. P. Chen, Y. Y. Shi, P. F. Tang, W. Q. Liao, *J. Am. Chem. Soc.* **2019**, *141*, 4474.
[34] W. Q. Liao, Y. Zhang, C. L. Hu, J. G. Mao, H. Y. Ye, P. F. Li, S. D. Huang, R. G. Xiong, *Nat. Commun.* **2015**, *6*, 7338.
[35] H.-Y. Ye, Y.-Y. Tang, P.-F. Li, W.-Q. Liao, J.-X. Gao, X.-N. Hua, H. Cai, P.-P. Shi, Y.-M. You, R.-G. Xiong, *Science* **2018**, *361*, 151.
[36] D.-W. Fu, H.-L. Cai, Y. Liu, Q. Ye, W. Zhang, Y. Zhang, X.-Y. Chen, G. Giovannetti, M. Capone, J. Li, *Science* **2013**, *339*, 425.
[37] W. Ke, L. Mao, C. C. Stoumpos, J. Hoffman, I. Spanopoulos, A. D. Mohite, M. C. Kanatzidis, *Adv. Energy Mater.* **2019**, *9*, 1803384.
[38] H. Tsai, W. Nie, J.-C. Blancon, C. C. Stoumpos, R. Asadpour, B. Harutyunyan, A. J. Neukirch, R. Verduzco, J. J. Crochet, S. Tretiak, *Nature* **2016**, *536*, 312.
[39] J. Fan, Y. Ma, C. Zhang, C. Liu, W. Li, R. E. I. Schropp, Y. Mai, *Adv. Energy Mater.* **2018**, *8*, 1703421.
[40] C. Ma, D. Shen, B. Huang, X. Li, W. C. Chen, M. F. Lo, P. Wang, M. H. W. Lam, Y. Lu, B. Ma, *J. Mater. Chem. A* **2019**, *7*, 8811.
[41] L. Gao, I. Spanopoulos, W. Ke, S. Huang, M. G. Kanatzidis, *ACS Energy Lett.* **2019**, *4*, 1763.
[42] Q. Jiang, L. Zhang, H. Wang, X. Yang, J. Meng, H. Liu, Z. Yin, J. Wu, X. Zhang, J. You, *Nat. Energy* **2016**, *2*, 16177.
[43] Z. Xiao, C. Bi, Y. Shao, Q. Dong, Q. Wang, Y. Yuan, C. Wang, Y. Gao, J. Huang, *Energy Environ. Sci.* **2014**, *7*, 2619.
[44] Q. Jiang, Z. Chu, P. Wang, X. Yang, H. Liu, Y. Wang, Z. Yin, J. Wu, X. Zhang, J. You, *Adv. Mater.* **2017**, *29*, 1703852.
[45] E. A. Alharbi, A. Y. Alyamani, D. J. Kubicki, A. R. Uhl, M. Grtzel, *Nat. Commun.* **2019**, *10*, 3008.
[46] P. Liu, Y. Xian, W. Yuan, Y. Long, K. Liu, N. U. Rahman, W. Li, J. Fan, *Adv. Energy Mater.* **2020**, *10*, 1903654.
[47] P. Chen, Y. Bai, S. Wang, M. Lyu, J. H. Yun, L. Wang, *Adv. Funct. Mater.* **2018**, *28*, 1706923.
[48] Y. Bai, S. Xiao, C. Hu, T. Zhang, X. Meng, H. Lin, Y. Yang, S. Yang, *Adv. Energy Mater.* **2017**, *7*, 1701038.
[49] Y. Yuan, J. Chae, Y. Shao, Q. Wang, Z. Xiao, A. Centrone, J. Huang, *Adv. Energy Mater.* **2015**, *5*, 1500615.
[50] W. E. I. Sha, X. Ren, L. Chen, W. C. H. Choy, *Appl. Phys. Lett.* **2015**, *106*, 221104.
[51] X. Ren, Z. Wang, W. E. I. Sha, W. C. H. Choy, *ACS Photonics* **2017**, *4*, 934.
[52] C. C. Zhang, Z. K. Wang, S. Yuan, R. Wang, M. Li, M. F. Jimoh, L. S. Liao, Y. Yang, *Adv. Mater.* **2019**, *31*, 1902222.
[53] E. Jia, D. Wei, P. Cui, J. Ji, H. Huang, H. Jiang, S. Dou, M. Li, C. Zhou, W. Wang, *Adv. Sci.* **2019**, *6*, 1900252.
[54] C. Peter, H. Kliem, *J. Appl. Phys.* **2019**, *125*, 174107.
[55] R. Nechache, C. Harnagea, S. Li, L. Cardenas, W. Huang, J. Chakrabartty, F. Rosei, *Nat. Photonics* **2015**, *9*, 61.

ADVANCED FUNCTIONAL MATERIALS

Supporting Information

for *Adv. Funct. Mater.,* DOI: 10.1002/adfm.202100205

Highly Efficient 1D/3D Ferroelectric Perovskite Solar Cell

Haijuan Zhang, Zejiao Shi, Laigui Hu, Yuan-Yuan Tang, Zhengyuan Qin, Wei-Qiang Liao, Zi Shuai Wang, Jiajun Qin, Xiaoguo Li, Haoliang Wang, Meenakshi Gusain, Fengcai Liu, Yiyi Pan, Mingsheng Xu, Jiao Wang, Ran Liu, Chunfeng Zhang, Ren-Gen Xiong, Wei E. I. Sha,* and Yiqiang Zhan**

Highly efficient 1D/3D ferroelectric perovskite solar cell

Haijuan Zhang[1]*, Zejiao Shi[1]*, Laigui Hu[1]*, Yuan-Yuan Tang[3], Zhengyuan Qin[4], Wei-Qiang Liao[3], Zi Shuai Wang[5], Jiajun Qin[1], Xiaoguo, Li[1], Haoliang Wang[1], Meenakshi Gusain[1], Fengcai liu[1], Yiyi Pan[1], Mingsheng Xu[1], Jiao Wang[1], Ran Liu[1], Chunfeng Zhang[4], Ren-Gen Xiong[2, 3]†, Wei E.I. Sha[6]†, Yiqiang Zhan[1]†

1. Center for Micro Nano Systems, School of Information Science and Technology (SIST), Fudan University, Shanghai 200433, P. R. China

2. Jiangsu Key Laboratory for Science and Applications of Molecular Ferroelectrics, Southeast University, Nanjing 211189, P. R. China.

3. Ordered Matter Science Research Center, Nanchang University, Nanchang 330031, P. R. China

4. National Laboratory of Solid State Microstructures, School of Physics, and Collaborative Innovation Center for Advanced Microstructures Nanjing University, Nanjing 210093, P. R. China.

5. Department of Electrical and Electronic Engineering, The University of Hong Kong, Pokfulam Road, Hong Kong, P.R. China

6. State Key Laboratory of Modern Optical Instrumentation, College of Information Science and Electronic Engineering, Zhejiang University, Hangzhou 310027, P.R. China

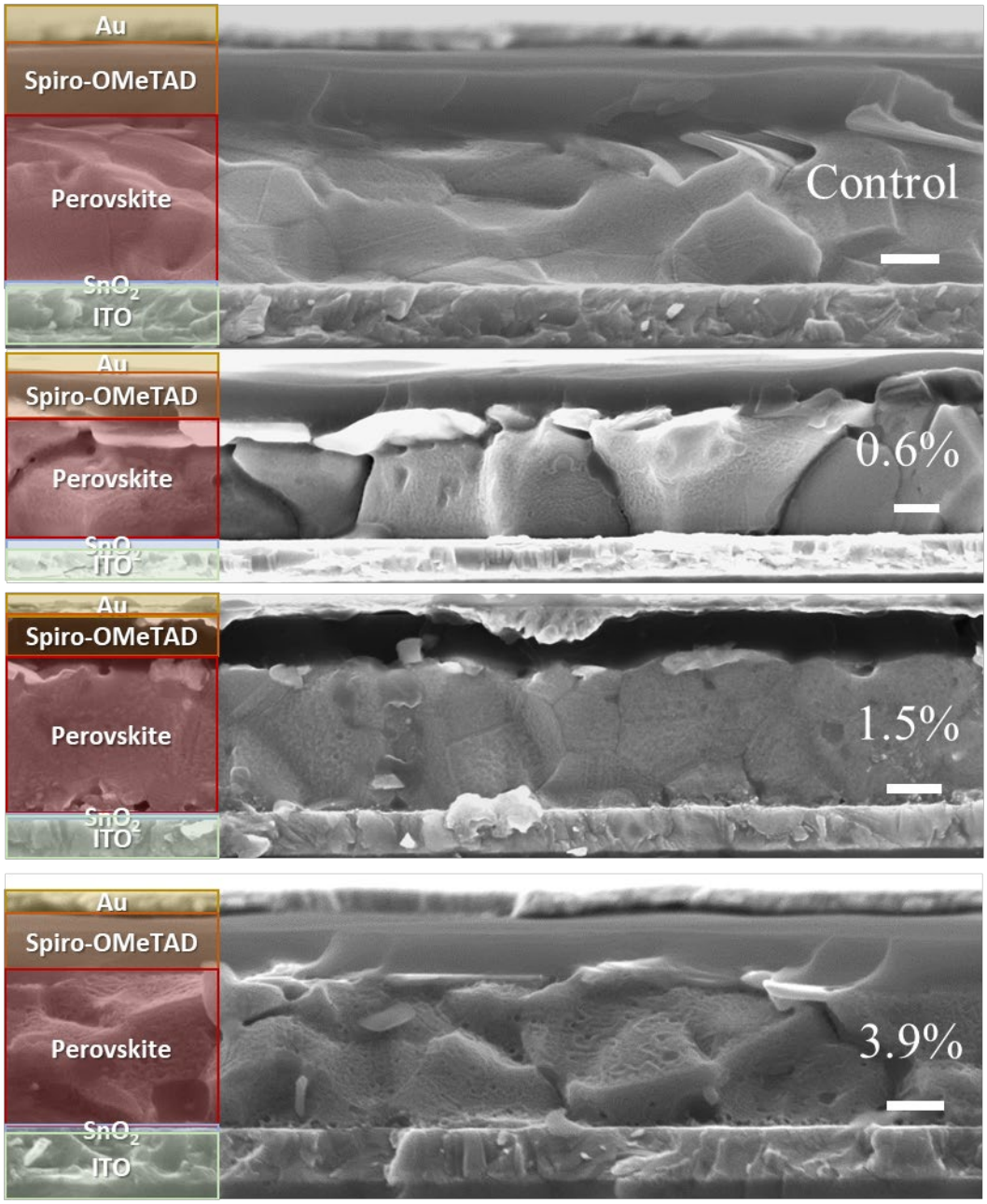

Figure S1. SEM cross section images of the control and different molar ratios 1D/3D mixed OIHP films. Scale bar: 0.2 μm. The thickness of perovskite layer is around 500 nm.

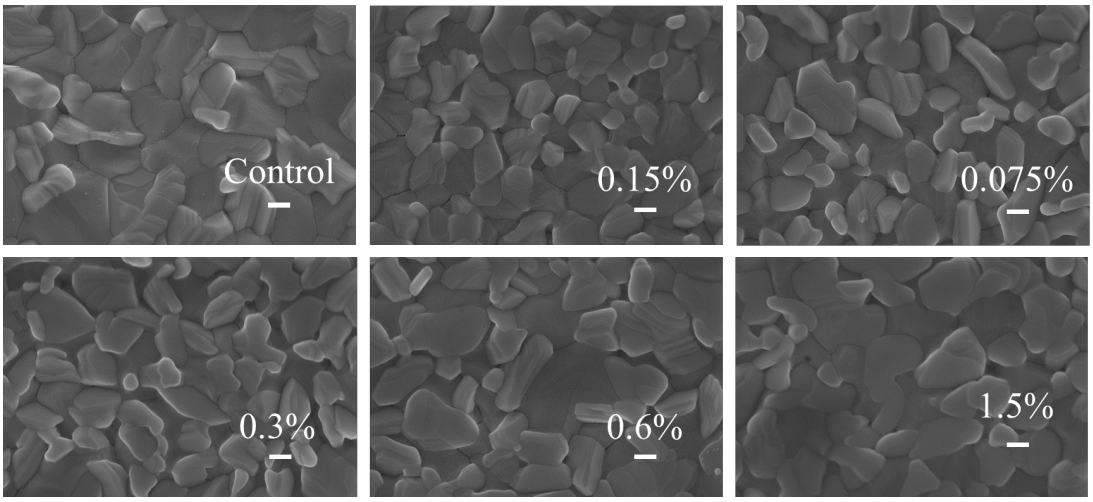

Figure S2. Top-view SEM images of the control and different mol ratios 1D/3D mixed OIHP films. Scale bar: 0.2 μm.

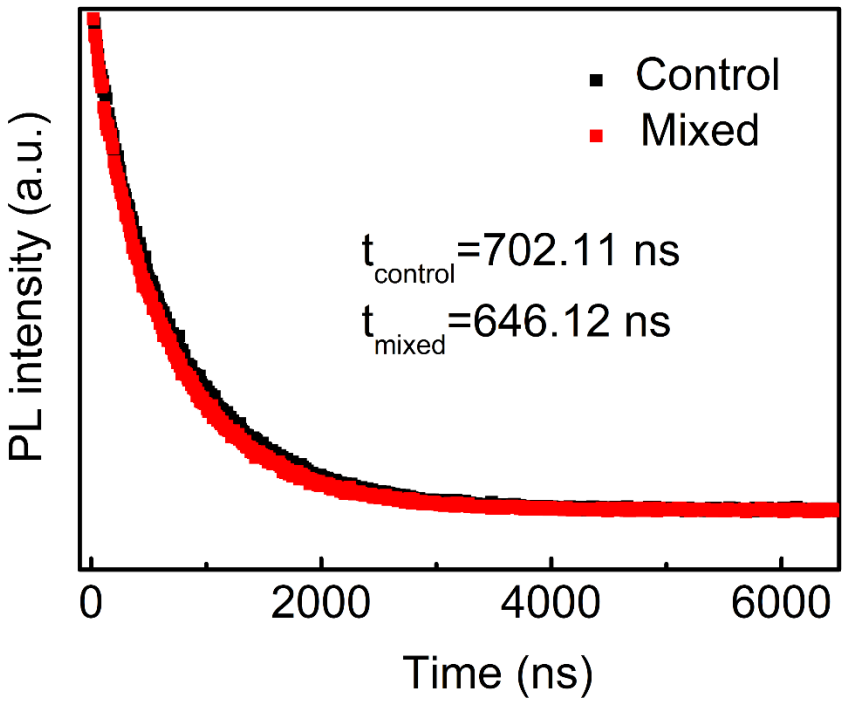

Figure S3. TRPL spectra of control and 1D/3D mixed OIHP films.

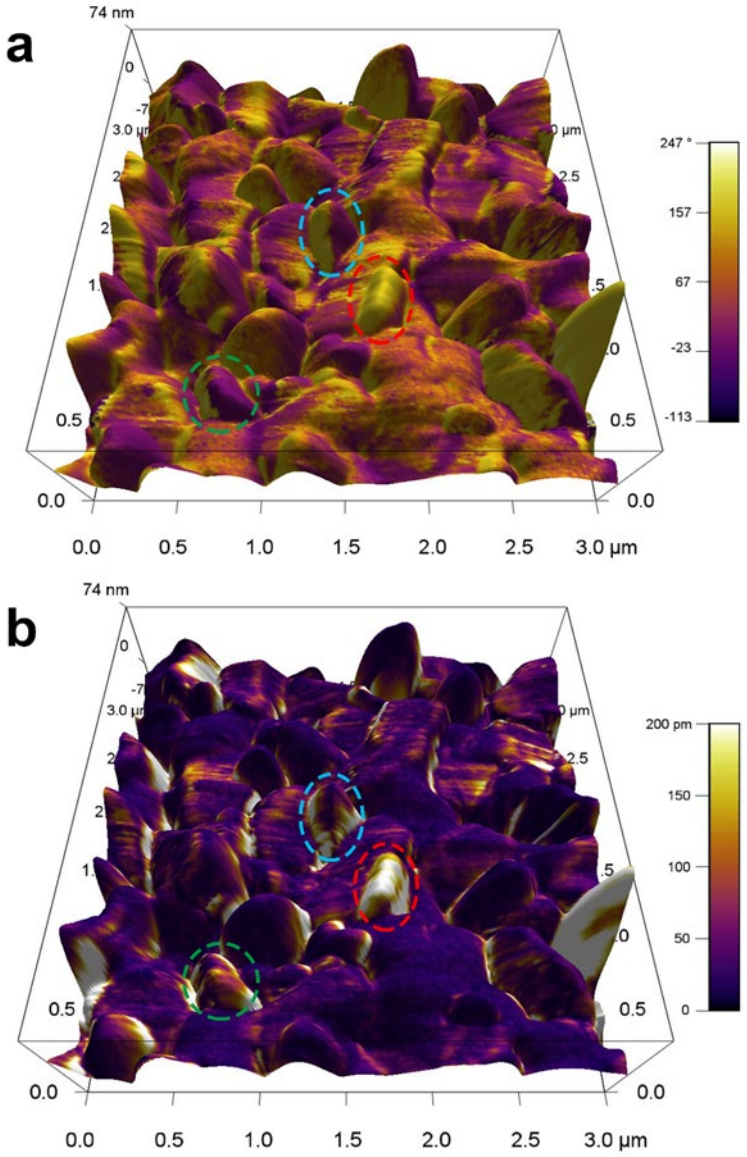

Figure S4. Phase mapping (a) and amplitude mapping (b) of the lateral PFM overlaid on the 3D topography for the thin film (1D/3D mixed OIHP). It is clear that the piezoresponse has no obvious correlation with the local topology of the sample surface. We chose three areas marked with dotted ellipses of different colors for detailed explanation. From the phase and amplitude images, we can see that the domain walls are not only at the highest boundary of the grain, but also at the left and right of the grains. Moreover, the adjacent domains on either side of domain walls have nearly equal amplitude signals, rather than that high amplitude signals occur on the same side of the grain. These results indicate there is no significant correlation between the contrast in both amplitude and phase images and the scan direction of the cantilever.

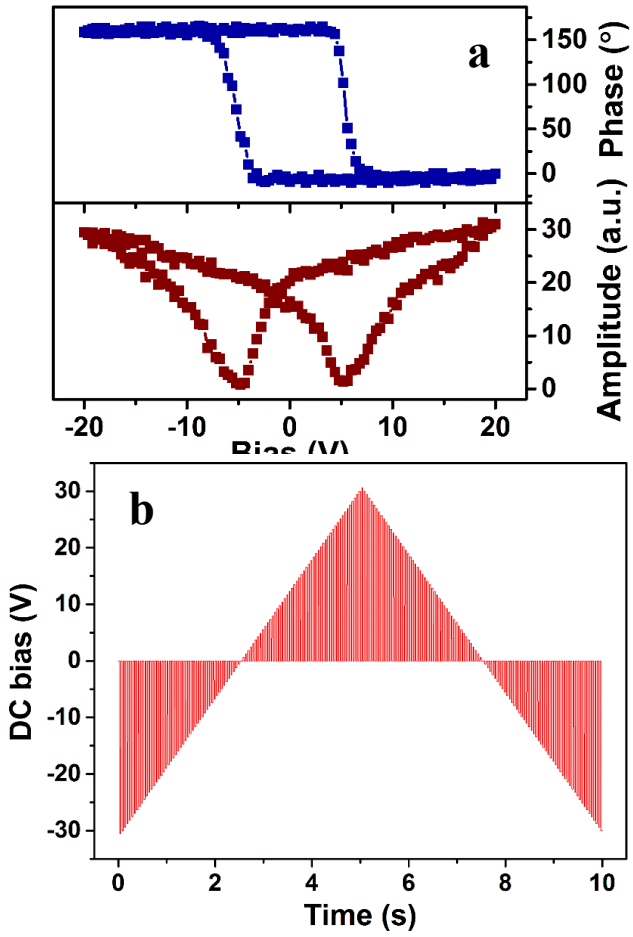

Figure S5. (a). Dependence of phase and amplitude signals with applied DC bias for a selected point on the 1.1 μm thin film (1D/3D mixed OIHP) on the ITO substrate when the sample is grounded, showing a hysteresis loop and a butterfly curve. The local coercive voltage is about 5 V, as indicated by the minima of the amplitude loop.

(b). In the hysteresis measurement shown in Figures. 2d and S5, an AC drive voltage is carried by a stepped DC bias voltage during the switching process. In order to minimized the electrostatic effect, the piezoresponse induced by V_{AC} is recorded after each step when V_{DC} = 0.

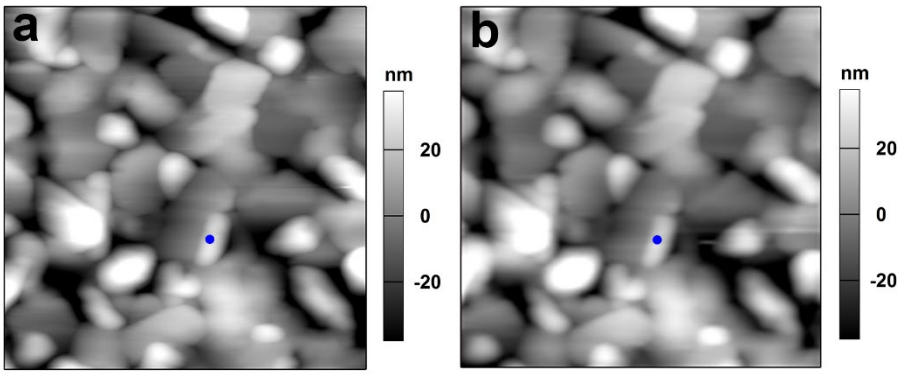

Figure S6. Topographic images of the thin film (1D/3D mixed OIHP) before (a) and after (b) the measurement of the hysteresis. The blue points indicate where the DC-sweep shown in Figure 2d was performed.

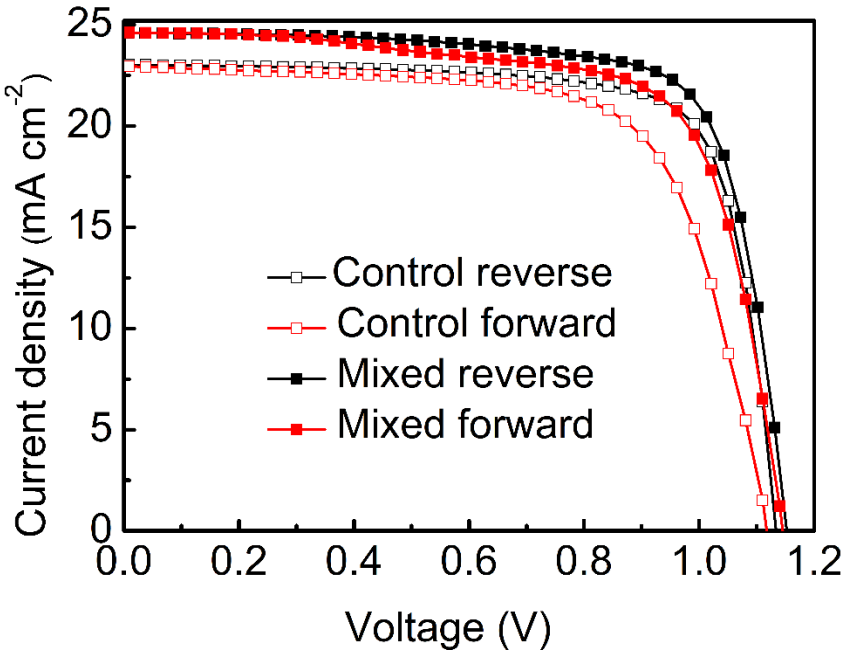

Figure S7. *J–V* curve obtained by reverse scan and forward scan for the control and 1D/3D mixed OIHP solar cell.

Table S1. J_{sc}, V_{oc}, *FF* ,*PCE* and Hysteresis parameters of control and 1D/3D mixed OIHP solar cell.

	J_{sc} (mA cm^{-2})	V_{oc} (V)	FF (%)	PCE (%)	Hysteresis Index
Control reverse	23.1	1.13	77	20.1	11.9%
Control forward	22.9	1.12	69	17.7	
Mixed reverse	24.6	1.15	75	21.2	5.2%
Mixed forward	24.6	1.15	71	20.1	

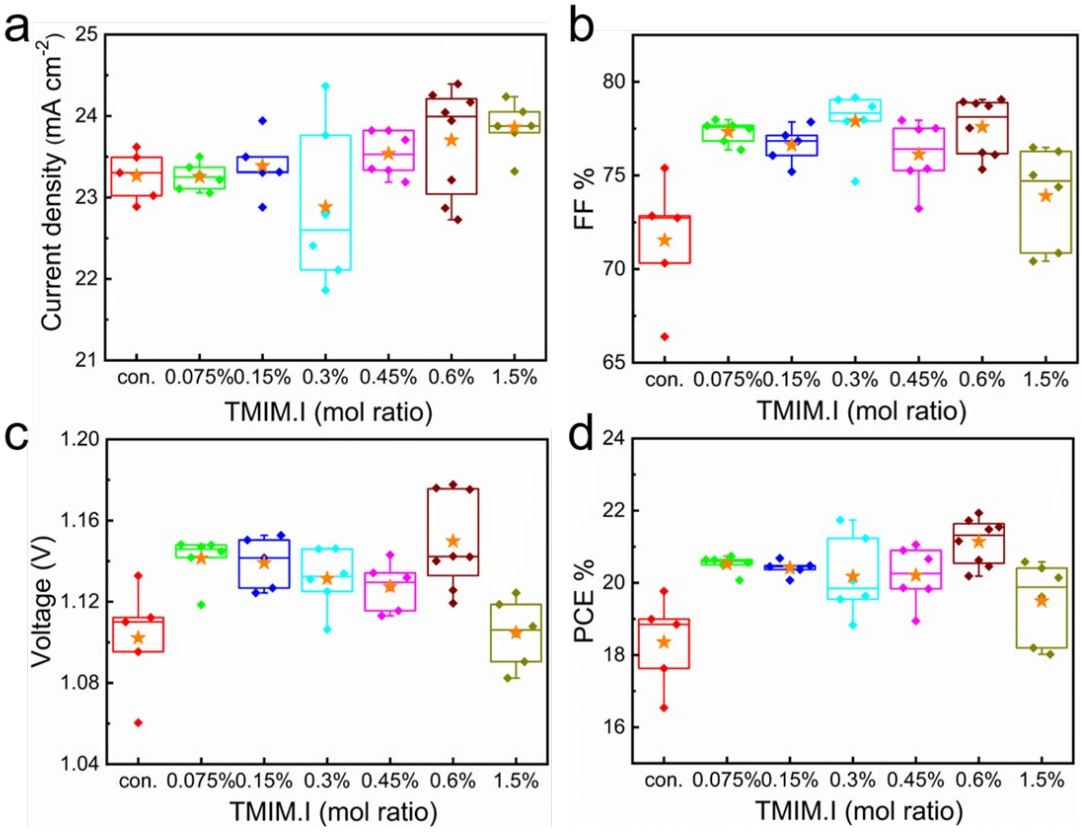

Figure S8. Statistics of J_{sc}, V_{oc}, *FF* and *PCE* parameters of control and different molar ratios of 1D perovskite phase in the 1D/3D mixed OIHP solar cells before poling.

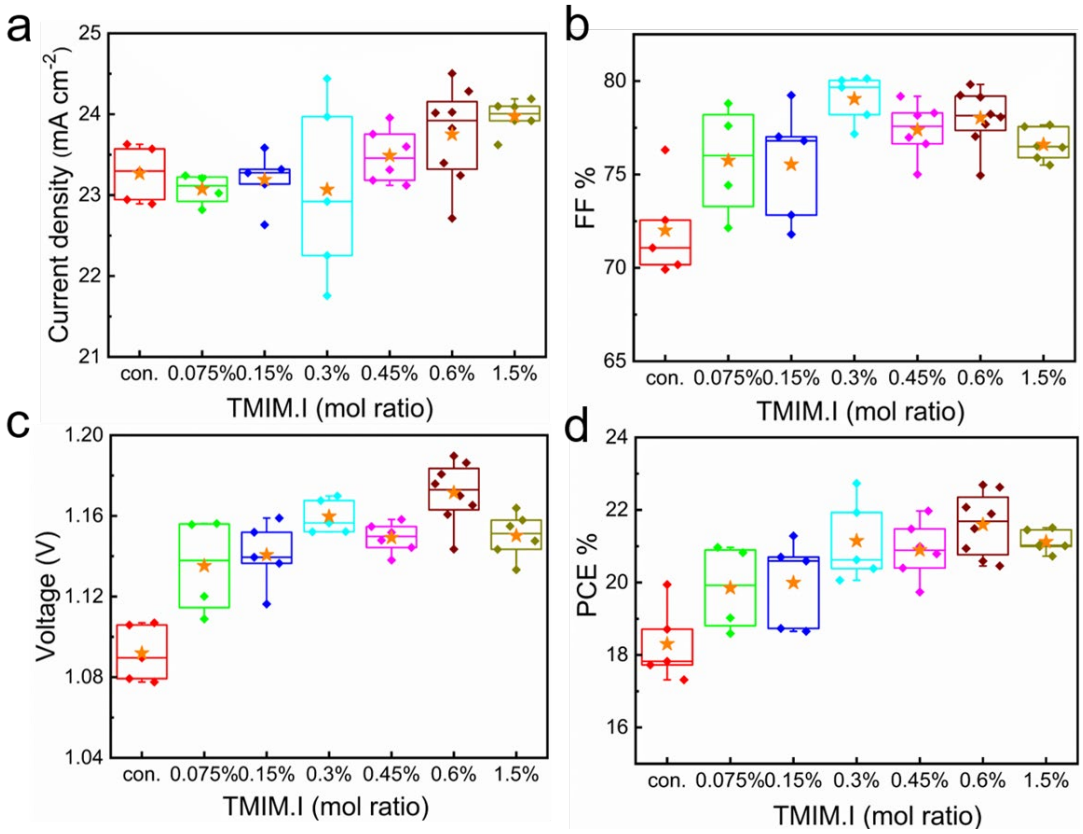

Figure S9. Statistics of J_{sc}, V_{oc}, *FF* and *PCE* parameters of control and different molar ratios of 1D perovskite phase in the 1D/3D mixed OIHP solar cells after poling.

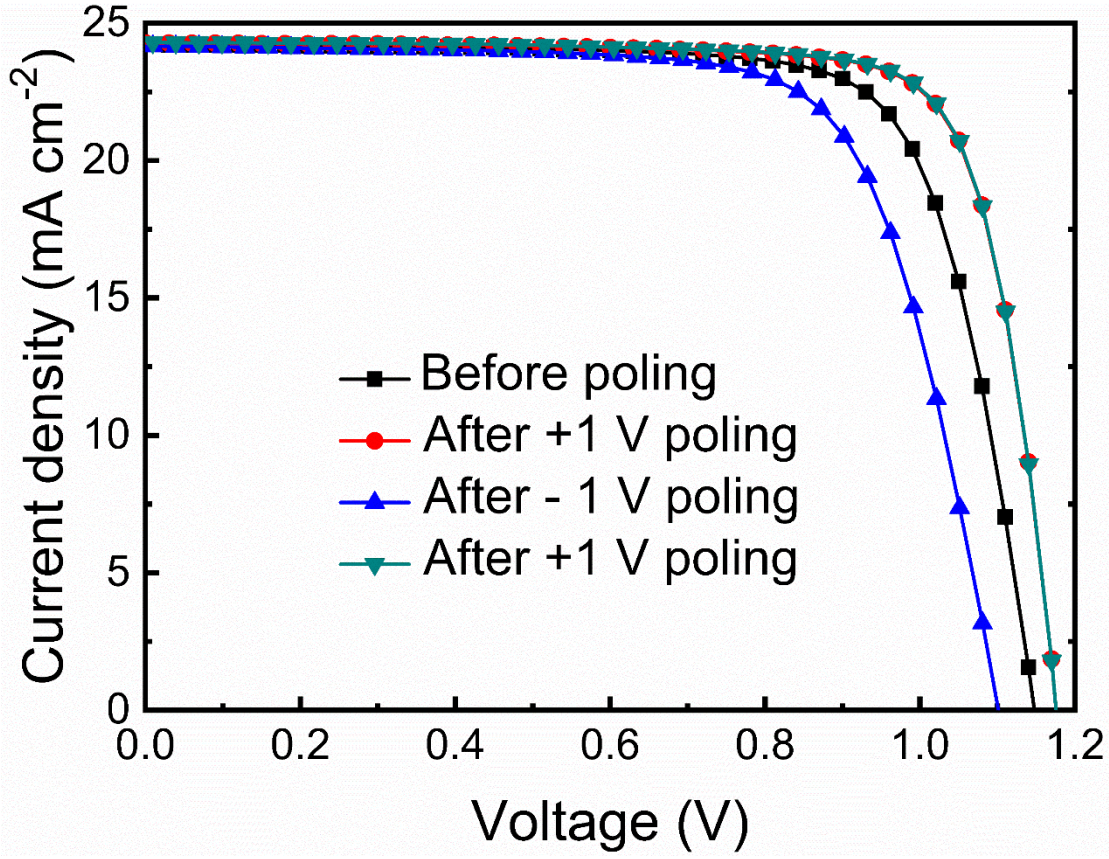

Figure S10. *J-V* curves of 1D/3D mixed OIHP solar cells before and after repeated poling.

Table S2. J_{sc}, V_{oc}, *FF* and *PCE* parameters of above 1D/3D mixed OIHP solar cells before and after poling.

	J_{sc} (mA cm^{-2})	V_{oc} (V)	FF (%)	PCE (%)
Before poling	24.2	1.15	75	21.0
After 1V poling	24.3	1.18	79	22.6
After -1V poling	24.2	1.10	72	19.1
After 1V poling	24.3	1.18	79	22.6

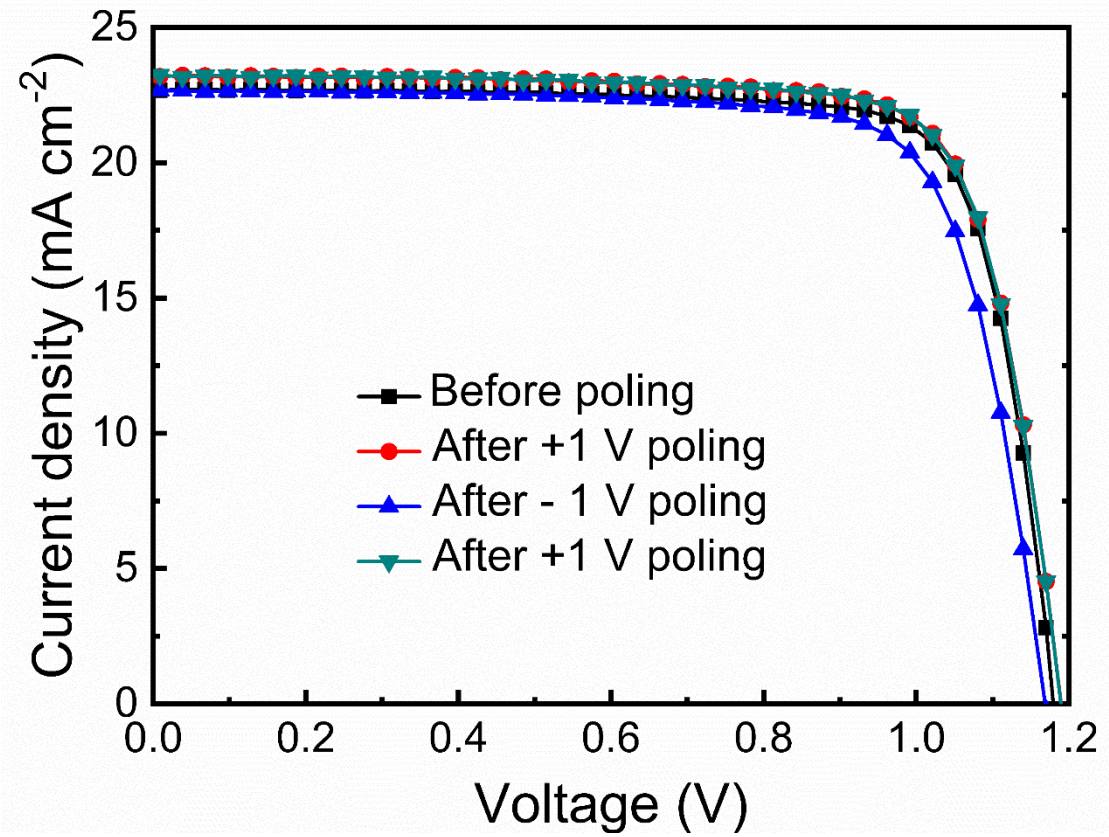

Figure S11. *J-V* curves of the champion Voc (1.19 V) for 1D/3D hybrid perovskite solar cells before and after repeated poling.

Table S3. J_{sc}, V_{oc}, *FF* and *PCE* parameters of above 1D/3D mixed OIHP solar cells before and after poling.

	J_{sc} (mA cm^{-2})	V_{oc} (V)	FF (%)	PCE (%)
Before poling	22.7	1.18	79	21.2
After 1 V poling	23.2	1.19	78	21.6
After -1 V poling	22.7	1.17	76	20.2
After 1 V poling	23.2	1.19	78	21.6

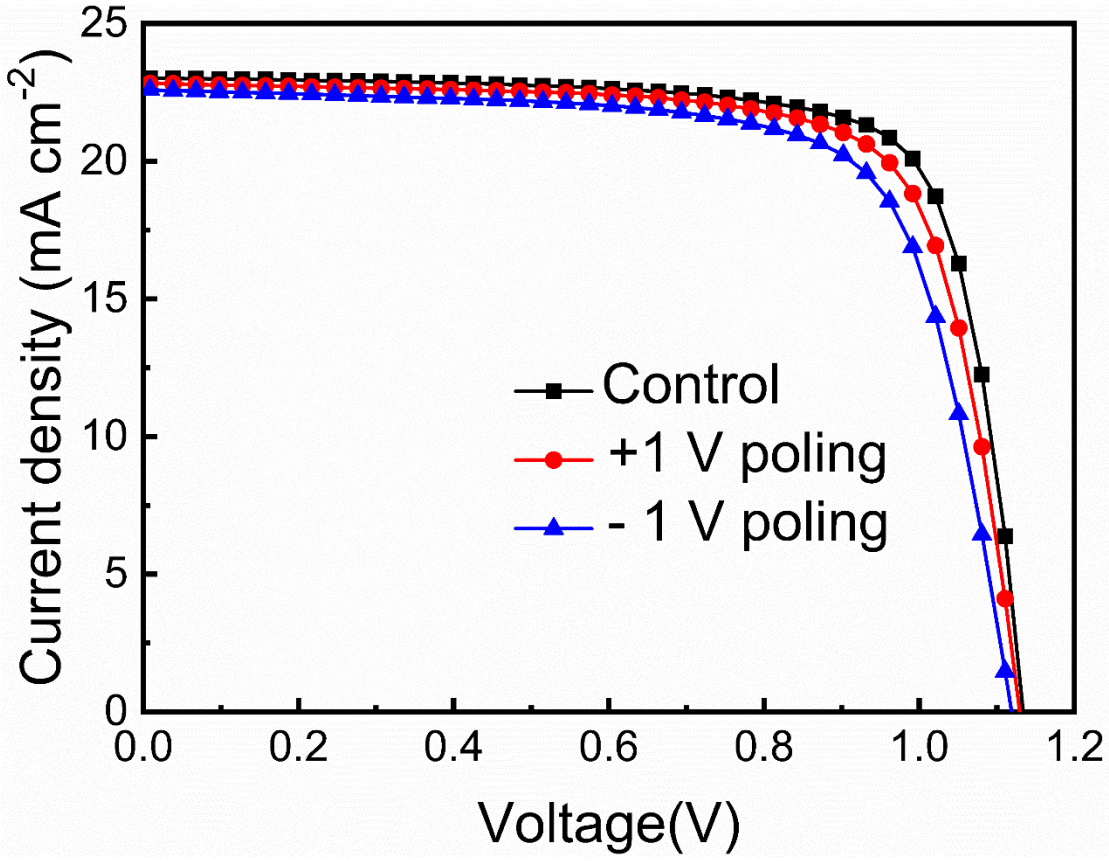

Figure S12. *J-V* curves of control OIHP solar cells before and after poling.

Table S4. J_{sc}, V_{oc}, *FF* and *PCE* parameters of the above control OIHP solar cells before and after poling.

	J_{sc} (mA cm^{-2})	V_{oc} (V)	FF (%)	PCE (%)
Before poling	23.0	1.13	77	20.1
After 1V poling	22.8	1.13	75	19.2
After -1V poling	22.6	1.12	72	18.2

The coercive field

To quantitively compare the coercive field in the device and in the PFM is not very easy. As the structures of devices and the thicknesses of perovskite films are both different. In the solar cells, there are the ETL and HTL in the device, and the thickness of perovskite is around 500 nm. The perovskite film for PFM measurement are directly deposited on ITO, with no ETL and HTL, and the thickness is over 1 μm. Furthermore, the shape of electric field in solar cells is different as the one in the PMF measurement, which might influence the coercive field as well.

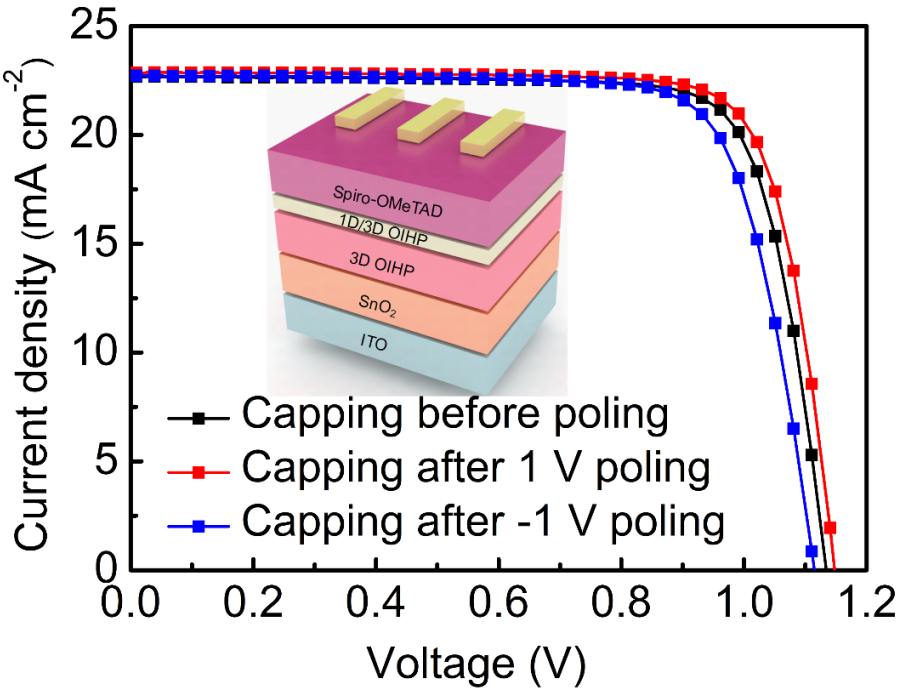

Figure S13. *J-V* curves of capping OIHP solar cells before and after poling.

Table S5. J_{sc}, V_{oc}, *FF* and *PCE* parameters of above capping OIHP solar cells before and after poling.

	J_{sc} (mA cm^{-2})	V_{oc} (V)	FF (%)	PCE (%)
Before poling	22.8	1.13	79	20.3
After 1 V poling	22.8	1.15	80	20.9
After -1 V poling	22.7	1.11	77	19.5

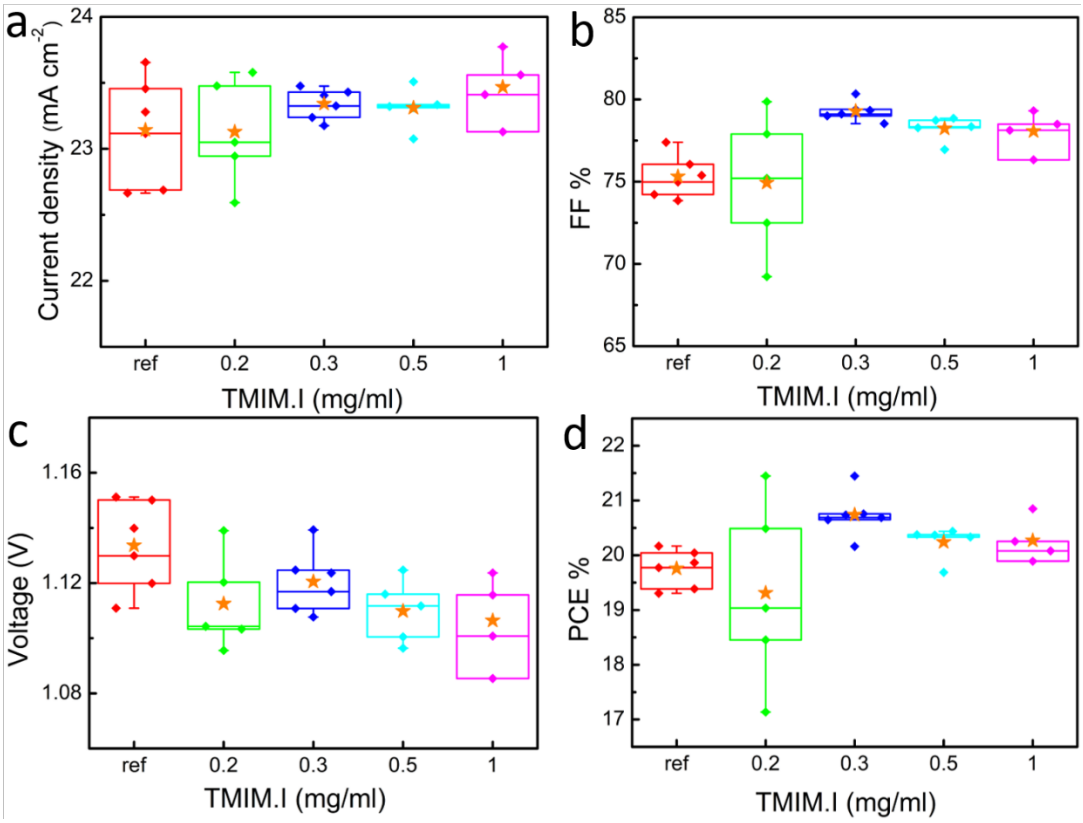

Figure S14. Statistics of J_{sc}, V_{oc}, *FF* and *PCE* parameters of control and different concentrations 1D/3D capping OIHP solar cells before poling.

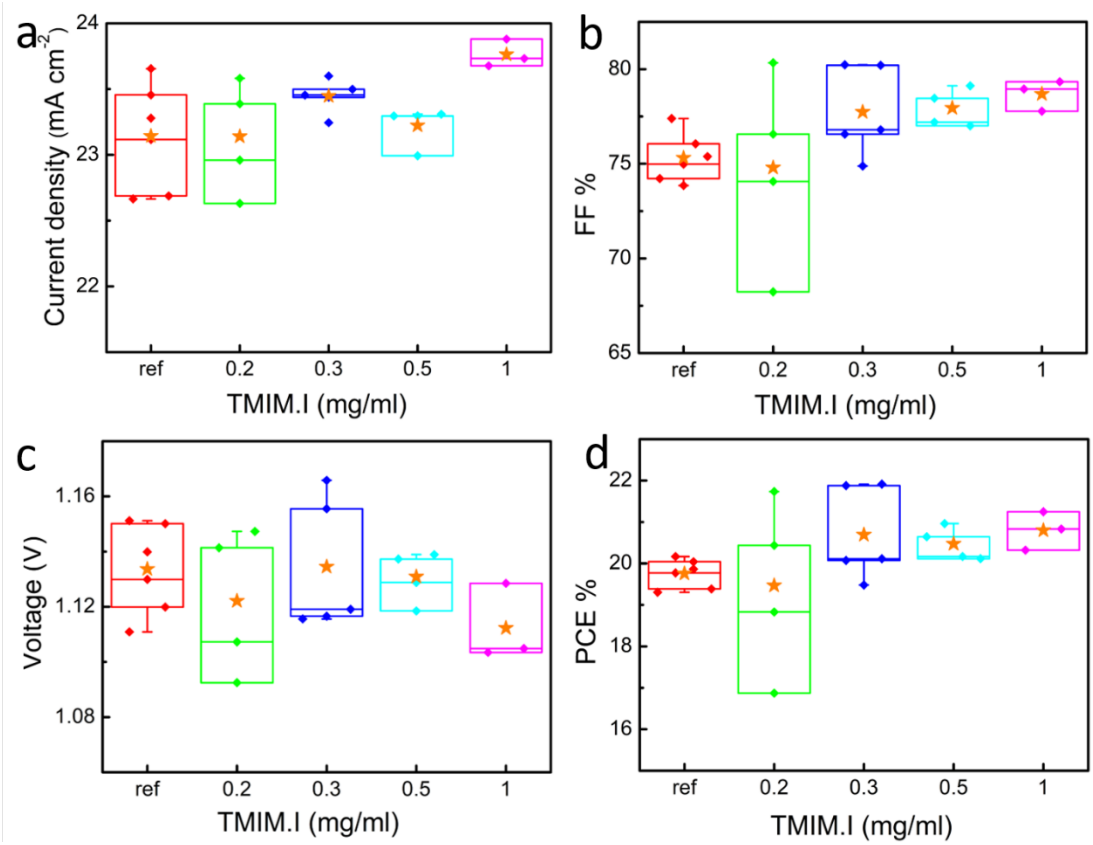

Figure S15. Statistics of J_{sc}, V_{oc}, *FF* and *PCE* parameters of control and different concentrations 1D/3D capping OIHP solar cells after poling.

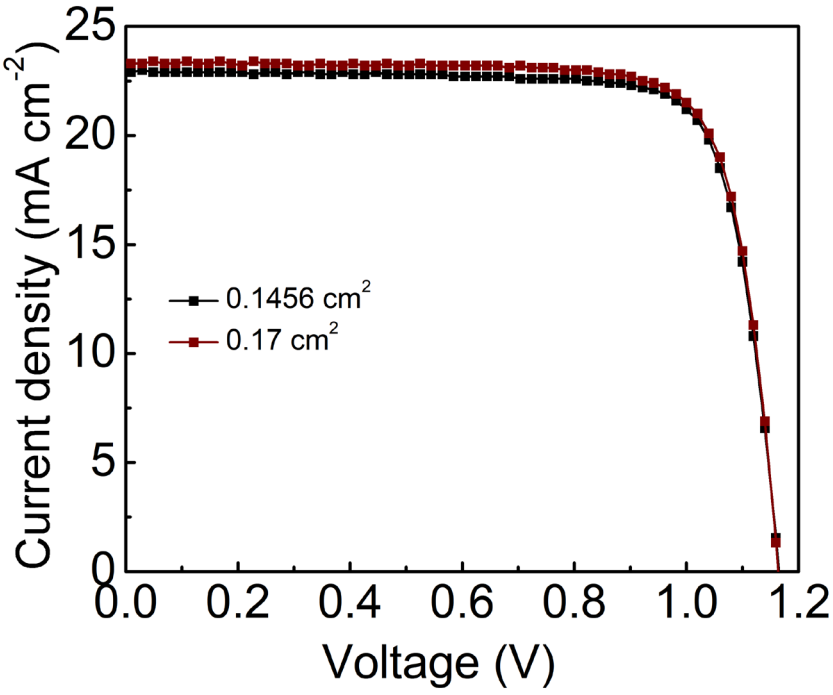

Figure S16. *J-V* characters of 1D/3D mixed OIHP solar cells after poling with (0.1456 cm^{-2}) and w/o (0.17cm^{-2}) aperture during testing.

Table S6. J_{sc}, V_{oc}, *FF* and *PCE* parameters of 1D/3D mixed OIHP solar cells after poling with (0.1456 cm^{-2}) and w/o (0.17cm^{-2}) aperture during testing.

Area (cm^2)	J_{sc} (mA cm^{-2})	V_{oc} (V)	FF (%)	PCE (%)
0.1456	22.9	1.17	80	21.3
0.17	23.3	1.16	79	21.6

Capacitance characteristics

A layer of 1D and 3D mixed perovskite film was deposited on the aluminum splitter finger electrode. The channel width of the split-finger electrode is 10 μm. The capacitance of 1D/3D mixed perovskite device before poling was measured under dark condition, with different frequency. And then the 1D/3D mixed perovskite device is polarized for 70 s at 18 V, which gives similar electric field as on the vertical device. The capacitance of the polarized 1D/3D mixed perovskite device was measured under the same condition. For the comparison, a control device with 3D perovskite and same structure are fabricated and measured. The results are shown in Figure S17.

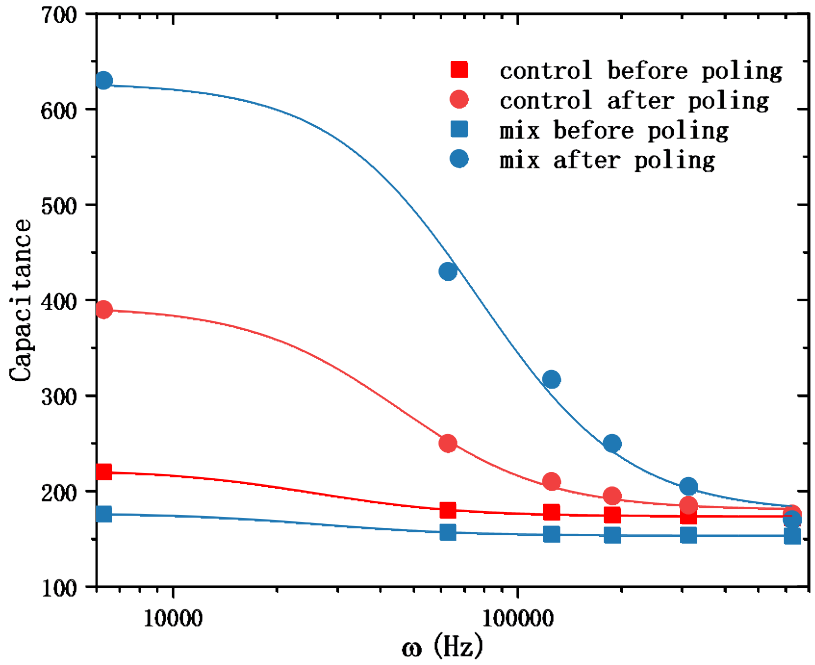

Figure S17. Capacitance measurement results and corresponding Debye models fitted for the control device and 1D/3D mixed device before and after poling. The Debye model is given by $C = C_0 \frac{\epsilon_s + \omega^2\tau^2\epsilon_\infty}{1+\omega^2\tau^2}$, where ϵ_s and ϵ_∞ are the static and high-frequency dielectric constants, respectively. τ is the relaxation time. ω is the angular frequency. The relationship between the angular frequency ω and the frequency f is: ω = 2 π f.

Table S7. Fitted Debye models for the control device and 1D/3D mixed device before and after poling.

	control before poling	**control after poling**	**mix before poling**	**mix after poling**
ϵ_s	222.76±2.23	393.80±5.29	177.25±0.56	627.97±17.3
ϵ_∞	173.75±1.02	180.54±3.16	153.54±0.27	177.54±12.8
τ	3.90e-5±7.24e-6	2.22e-5± 1.40e-6	3.76e-5 ± 3.57e-6	1.30e-5 ± 1.13e-6

Drift-diffusion simulation

The drift-diffusion simulation was conducted by our home-made transient drift-diffusion model. The governing equations of this model include:

$$\frac{\partial n}{\partial t} = \frac{1}{q}\frac{\partial J_n}{\partial x} + G - R \quad \text{(S1)}$$

$$\frac{\partial p}{\partial t} = -\frac{1}{q}\frac{\partial J_p}{\partial x} + G - R \quad \text{(S2)}$$

$$\frac{\partial a}{\partial t} = -\frac{1}{q}\frac{\partial J_a}{\partial x} \quad \text{(S3)}$$

$$\frac{\partial^2 V}{\partial x^2} = -\frac{q}{\varepsilon_0 \varepsilon_r}(n - p - a + N_{static} + N_A - N_D) \quad \text{(S4)}$$

where Equations S1-S3 are the continuity equations of electron (n), hole (p), and positive mobile ion (a), and Equation S4 is the Poisson's equation. N_{static} is the negative immobile ion and N_A and N_D are the doping densities for buffer layers. G and R refer to the generation rate and recombination rate, respectively, where the generation rate used in this simulation study is uniform in the absorber and the recombination includes radiative recombination, SRH recombination, as expressed below:

$$R_{rad} = k_{rad}(np - n_{in}^2) \quad \text{(S5)}$$

$$R_{SRH} = \frac{np - n_i^2}{\tau_n(p + p_t) + \tau_p(n + n_t)} \quad \text{(S6)}$$

Capture cross-section and density of the trap are represented by the reciprocal of their product, SRH lifetime $\tau_{n(p)}$, which is more intuitional and directly related to the lifetime measured in transient photoluminescence study. If the surface recombination is needed in the simulation study, the defect-assisted surface recombination will be set into SRH type as:

$$R_{surf} = \frac{n^+ p^- - n_i^2}{\tau_{surfn}(p^- + p_t) + \tau_{surfp}(n^+ + n_t)} \quad \text{(S7)}$$

where n^+ and p^- are the electron and hole densities on the two sides of the interface, respectively, and $\tau_{surfn(p)}$ donates the surface recombination lifetime, which is physically related to the reciprocal of the product of surface defect density and its capture cross section. The surface recombination R_{surf} will be added in Eqs. S1-S2 in addition to R_{SRH}.

The drift-diffusion current terms in the continuity equations are:

$$J_n = q\mu_n\left(n\frac{d\psi_n}{dx} + k_B T\frac{dn}{dx}\right) \quad \text{(S8)}$$

$$J_p = q\mu_p\left(p\frac{d\psi_p}{dx} - k_B T\frac{dp}{dx}\right) \quad \text{(S9)}$$

$$J_a = q\mu_a\left(a\frac{dV}{dx} - k_B T\frac{da}{dx}\right) \quad \text{(S10)}$$

Carrier mobilities of electron, hole, and positive mobile ion are μ_n, μ_p, μ_a, respectively, and Einstein's relation is implicitly included. T is temperature, and k_B is Boltzmann constant. It is worth noting that the potential terms in Equations S8-

S9, $\psi_{n/p}$, and in Equation S10, V, are different, as $\psi_{n/p}$ includes the effect from the energy band structures, expressed as:

$$\psi_n = V + \frac{\chi}{q} + \frac{k_B T}{q}\ln(N_c) \qquad \text{(S11)}$$

$$\psi_p = V + \frac{\chi}{q} + \frac{E_g}{q} - \frac{k_B T}{q}\ln(N_V) \qquad \text{(S12)}$$

For continuity equations of electron and hole, current boundary conditions are applied, as:

$$J_{nc} = S_{nc}(n - n_{0c}) \qquad \text{(S13)}$$

$$J_{na} = S_{na}(n - n_{0a}) \qquad \text{(S14)}$$

$$J_{pc} = S_{pc}(p - p_{0c}) \qquad \text{(S15)}$$

$$J_{pa} = S_{pa}(p - p_{0a}) \qquad \text{(S16)}$$

where S_{nc}, S_{pa}, S_{na}, S_{pc} are surface recombination velocities, and n_{0c}, n_{0a}, p_{0c}, p_{0a} are the boundary values of electron and hole densities at the electrodes, determined by the Schottky barriers. Infinite large surface recombination velocities for majority carriers (S_{nc}, S_{pa}) and zero surface recombination velocities for minority carriers (S_{np}, S_{pc}) represent the perfectly selective contacts.

For the continuity equation of positive mobile ion, Dirichlet boundary condition is applied, indicating the contacts are insulating for ionic carriers:

$$\mathrm{a(x = 0) = a(x = d) = 0} \qquad \text{(S17)}$$

where x=0 and x=d represent the spatial grids at cathode and anode, and d refers to the thickness of the device. What insulates the transport of mobile ion across the perovskite/CTL interface is the zero mobility in the CTL.

For Poisson's equation, we also apply the Dirichlet boundary condition:

$$\mathrm{V(x = 0)} = -WF_{cathode} \qquad \text{(S18)}$$

$$\mathrm{V(x = d)} = V_{app} - WF_{anode} \qquad \text{(S19)}$$

where $WF_{cathode/anode}$ is the work function of cathode or anode, and V_{app} is the externally applied voltage.

The continuity equations were discretized in space domain by S-G scheme [1], and in time domain by backward Euler's method. These equations were solved sequentially in Gummel's iteration and the converged solutions were obtained in each time step.

Through the post-processing of the converged solution of the proposed model at specific applied voltage, we can directly plot the potential distribution as the solution of Poisson's equation (**Figure 5**a), from which we can also calculate the electric field results (**Figure 5**d). Recombination rate distribution can be obtained from the electron and hole density distributions based on the recombination equations Eqs. S5-S7 (**Figure 5**b). By sweeping the applied voltage, we will have the evolution of current density at the electrodes and plot the J-V curves as shown in **Figure 5**c.

For simplification and approximation, symmetric modeling structures were used and the input parameters were extracted from other studies or selected in the

realistic region. The device structure of p-i-n is applied in the simulation study, where the ETL and HTL are set as perfect selective CTLs with high majority carrier mobility and low minority carrier mobility. High enough blocking energetic band offsets are also set for better selectivity, whereas the surface recombination will exist at the interfaces between the CTLs and perovskite if necessary. Carrier generation rate is uniformly distributed in the absorber with the approximated value which ensures the simulated Jsc can be compared with the experiments.

Table S8. Parameters used in the drift-diffusion simulation

Parameter Names	**Symbols [units]**	**Values**		
		ETL	**Absorber**	**HTL**
Bandgap	Eg [eV]	2.3	1.6 [2]	2.3
Thickness	L [nm]	200	500	200
Electron affinity	χ [eV]	4.1	3.8	2.8
Effective Fermi level	E0 [eV]	4.2	4.6	5.0
SRH lifetime for electron and hole	T [μs]	Inf large	1 [0.1 for surface if applicable]	Inf large
Nominal radiative recombination coefficient	k_{rad} [cm^3/s]	$1.5*10^{-10}$	$3.6*10^{-12}$	$1.5*10^{-10}$
Electron mobility	μ_n [cm^2/Vs]	20	2 [3]	0
Hole mobility	μ_p [cm^2/Vs]	0	2 [3]	20
Cation mobility	μ_a [cm^2/Vs]	0	10^{-9}	0
Initial cation density	a [$/cm^3$]	0	10^{18} [4]	0
Generation rate	G [$/m^3s$]	0	$3*10^{27}$	0
Density of state	$N_{c/v}$ [$/cm^3$]	10^{19}	10^{19}	10^{19}
Relative dielectric constant	ε_r	4	31 [5]	4
Schottky barrier	B_n, B_p [eV]	0.1	--	0.1

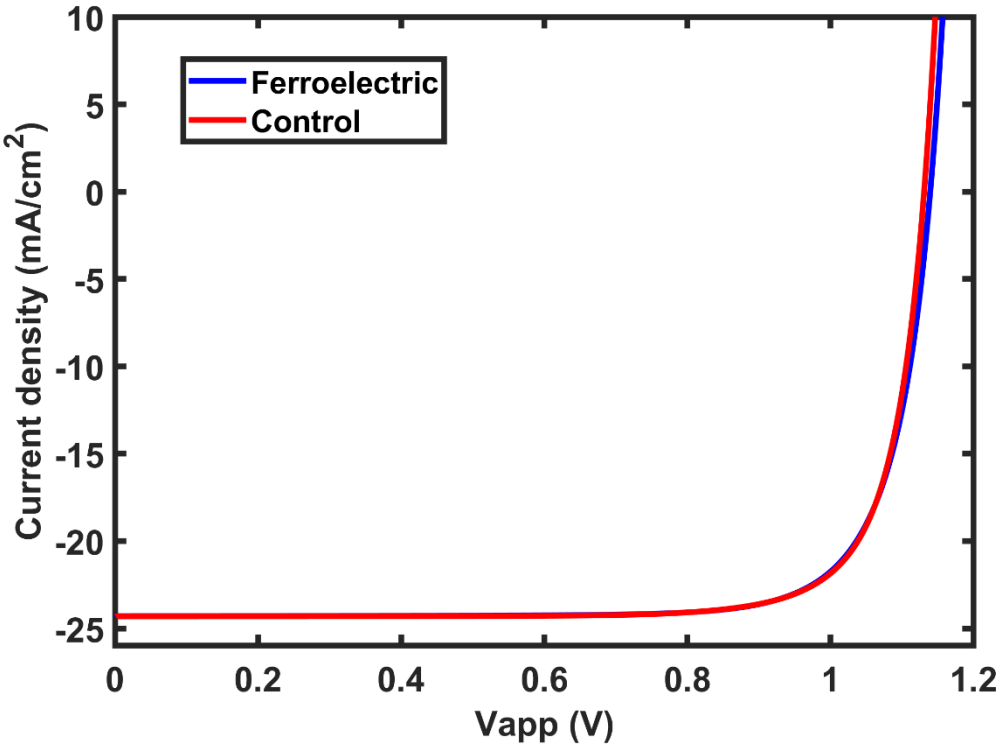

Figure S18. Compare of simulated *J-V* curves of control and ferroelectric PSCs with negligible interfacial recombination.

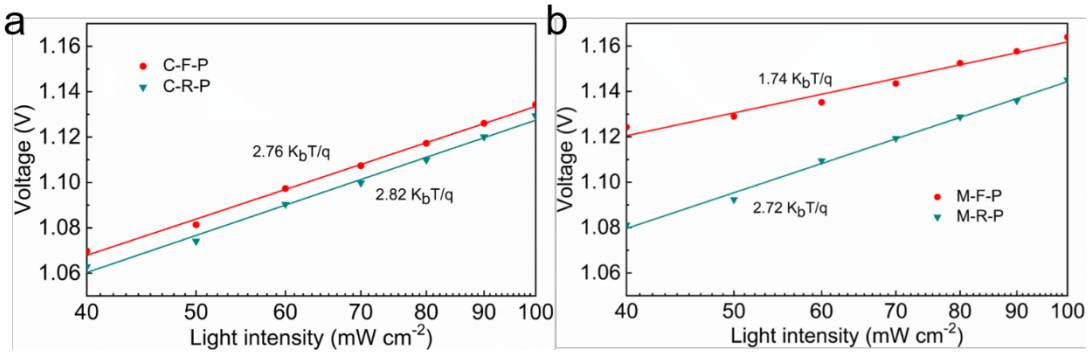

Figure S19. (a) V_{oc} versus light intensity for control PSCs with positive and negative poling. C-F-P: Control PSCs forward poling. C-R-P: Control PSCs reverse poling. (b) V_{oc} versus light intensity for 1D/3D mixed PSCs with positive and negative poling. M-F-P: Mixed PSCs forward poling. M-R-P: Mixed PSCs reverse poling. The lines in the figure are guide for the eye.

The fitting curves was performed via using the Equation (2),

$$V_{oc} = (nK_{\mathrm{B}}Tq^{-1})\ln(J_{sc}/J_0 + 1) \quad (2)$$

where n is the ideal factor, K_B is Boltzmann constant, T is temperature, q is elementary charge and J_0 is saturated dark current density. According J_0 is negligible compared with J_{sc} and J_{sc} is proportional to light intensity, the equation could be simplified as $V_{\mathrm{oc}} \propto nK_BT/q$. Relatively lower n value of 1.74 for 1D/3D mixed PSCs with positive poling (2.72 with negative poling), where an ideal trap-free system tend to close to 1, illustrates reduced trap-assistant recombination.

Low temperature polarization

A *J-V* characteristic before/after poling at room/low temperature of control (a) and 1D/3D mixed (b) PSCs have been studied systematically, to exclude the effect of ion migration.

The result in Figure S20a shows that there is no observable change of the *J-V* curves in control device after positive or negative polarization at 250 K. However, in ferroelectric PSCs even without ion migration, the current before and after poling will still differ much, indicating polarization field is contributed by ferroelectric property of 1D/3D mixed OIHP.

Furthermore, the zero of current indicates the zero of the total electric field. From Figure S20a, in the control device, at room temperature, the zero point changes in a very small range, generated by the mobile ions. However, in the ferroelectric device, the zero point has changed a lot more, which proves that the electric field arising from ferroelectric polarization is much higher than that from mobile ions.

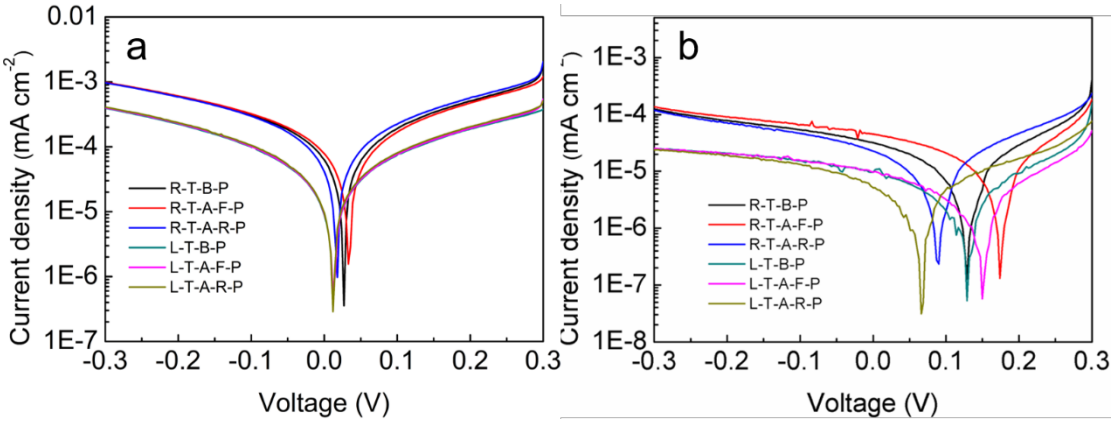

Figure S20. *J-V* characteristic before/after poling at room/low temperature of control (a) and 1D/3D mixed (b) PSCs. R-T-B-P: Room temperature before poling. R-T-A-F-P: Room temperature after forward poling. R-T-A-R-P: Room temperature after reverse poling. L-T-B-P: Low temperature before poling. L-T-A-F-P: Low temperature after forward poling. L-T-A-R-P: Low temperature after reverse poling.

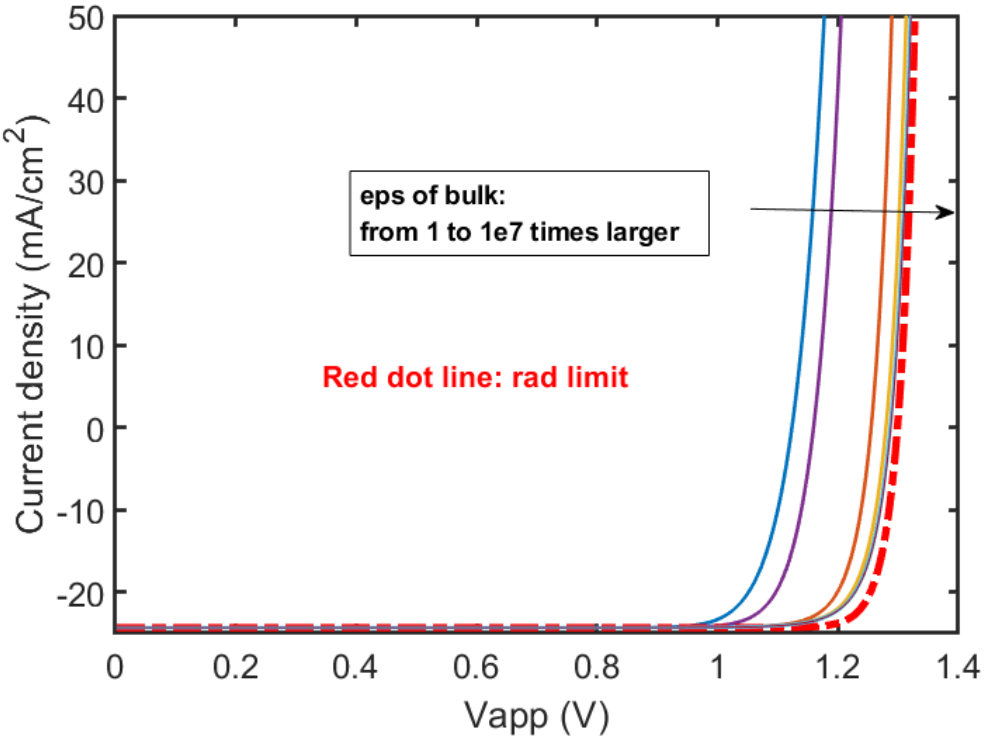

Figure S21. The simulated *J-V* characteristics of the ferroelectric PSCs with extremely large bulk dielectric constants.

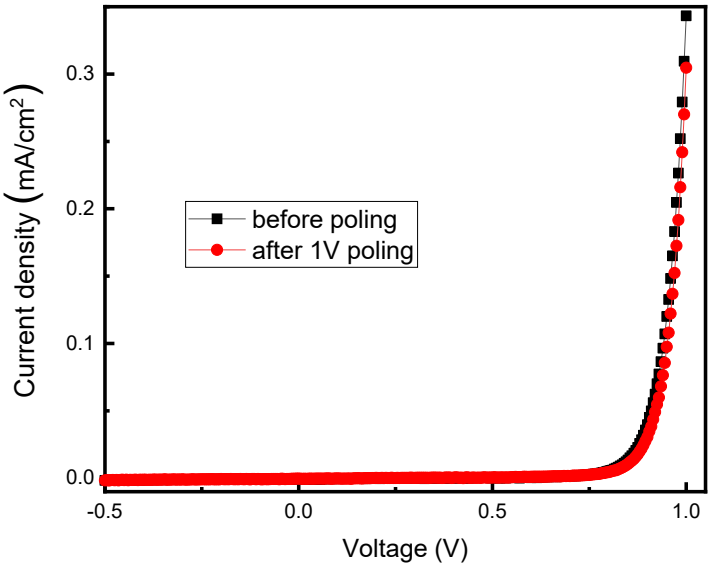

Figure S22. *J-V* curves under dark condition of 1D/3D mixed OIHP solar cell before and after poling.

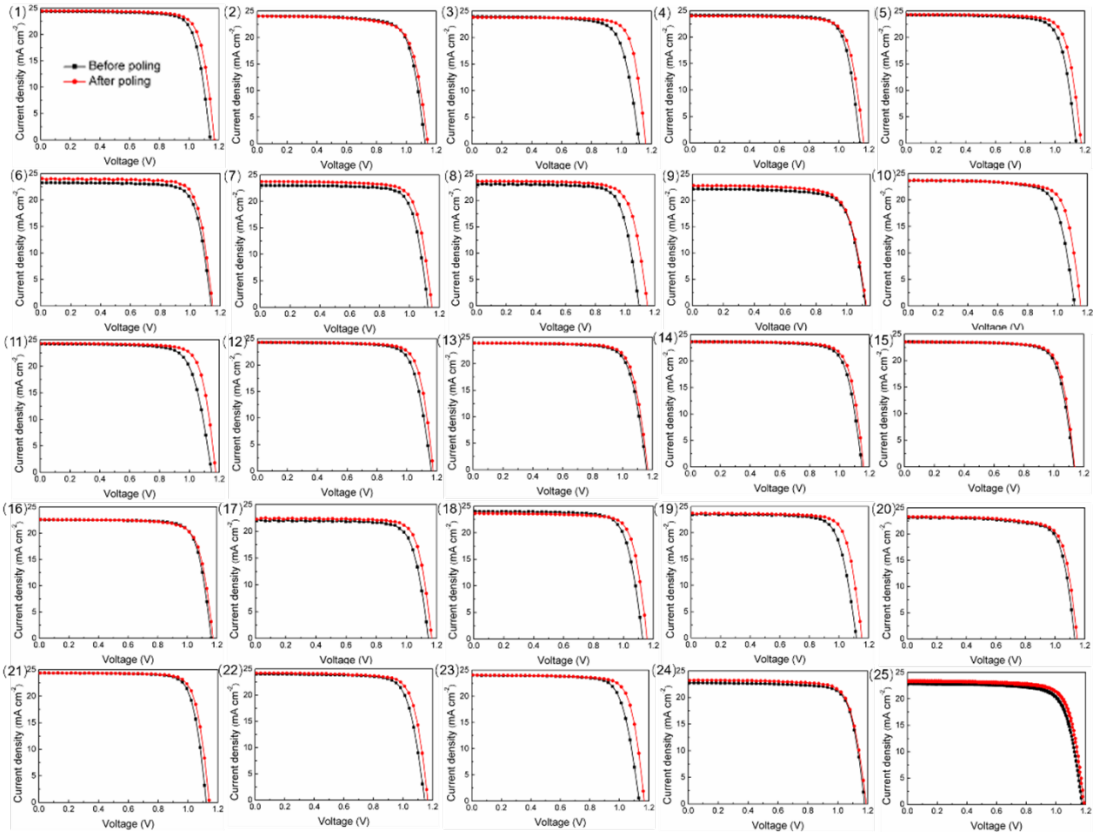

Figure S23. *J-V* curves of all 1D/3D mixed PSCs before and after poling which shown in Figure 3f.

TRPL and PL measurements

A layer of 1D/3D mixed perovskite film was deposited on the aluminum splitter finger electrode. The channel width of the split-finger electrode is 10 μm. TRPL and PL data of control device and 1D/3D mixed device were measured before and after poling. The 1D/3D mixed perovskite device is polarized for 70 s at 18 V, which gives similar electric field as on the vertical device. In the control device, there is no obvious change in TRPL or PL data. However, the PL lifetime of the 1D/3D mixed ferroelectric perovskite film is clearly increased, with a red shift of PL peak. This is a solid evidence, proving the intrinsic radiative recombination rate can be reduced by the ferroelectric polarization field.

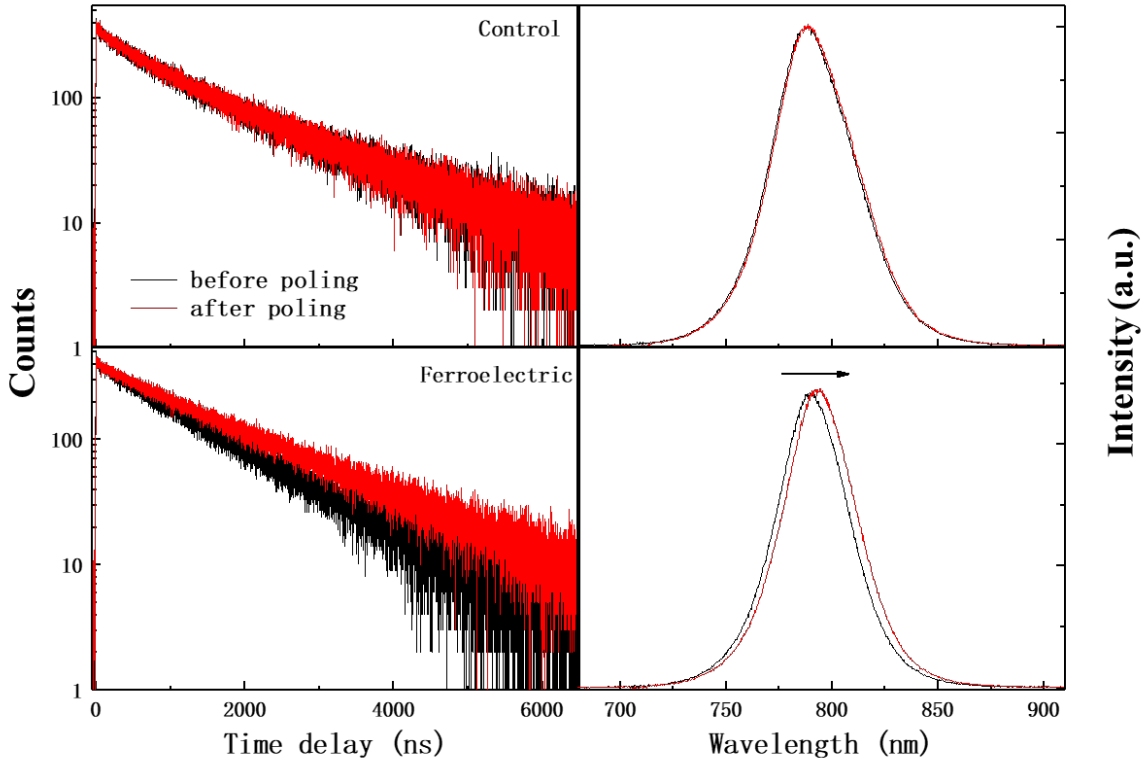

Figure S24. TRPL and PL data of control device and 1D/3D mixed device before and after poling.

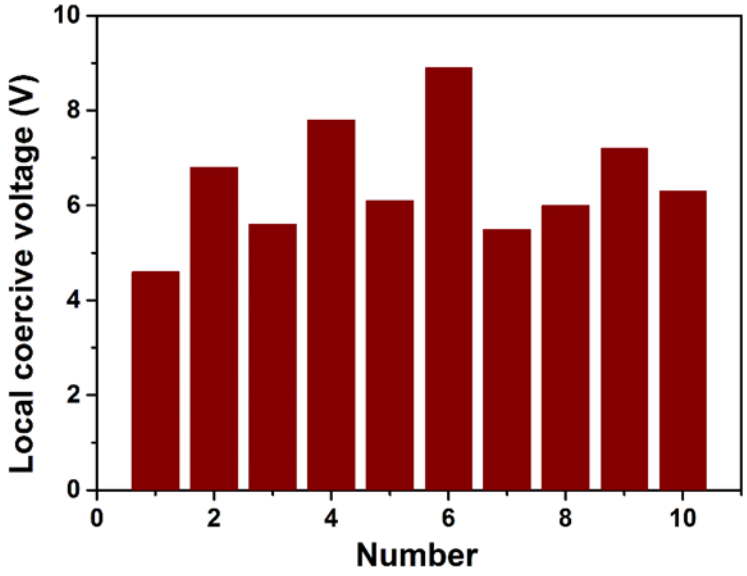

Figure S25. The local coercive voltages for ten selected points in the grains with strong amplitude signals on the thin film (1D/3D mixed OIHP) when the sample is grounded. The local coercive voltage ranges from 4.6 to 8.9 V, with an average of 6.5 V, as indicated by the minima of the amplitude loop.

We have chosen ten positions in the grains with strong amplitude signals on the 1D/3D mixed OIHP film to carry out new local PFM-based hysteresis loop measurements in the revised version. All of them can show 180° phase hysteresis loops and typical butterfly-shape amplitude loops, indicating the good reproducibility of PFM phase and amplitude switch data. Figure S1 exhibits the corresponding local coercive voltages, ranging from 4.6 to 8.9 V, with an average of 6.5 V, as indicated by the minima of the amplitude loop. For polycrystalline films, the local coercive voltages are often different in various places on a surface, due to the anisotropy of different grains.

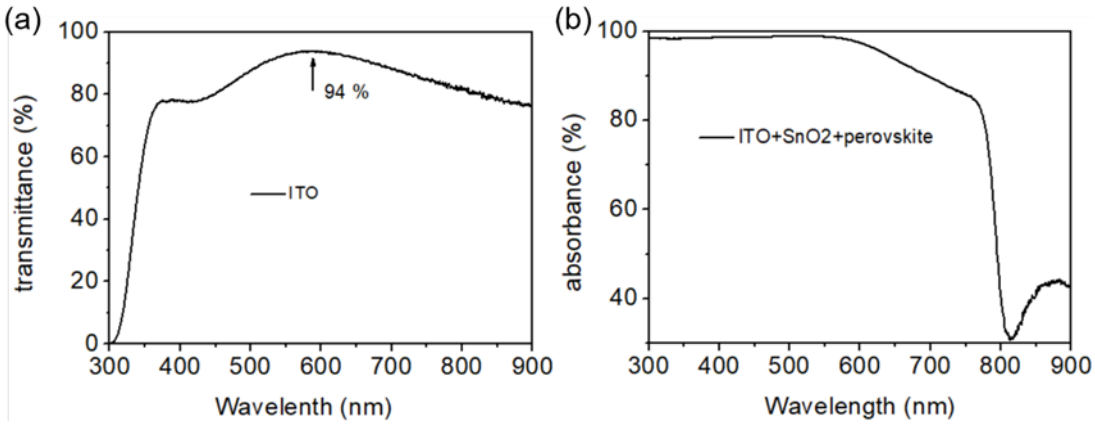

Figure. S26 (a) Transmission spectrum of ITO substrates in manuscript; (b) Absorption spectrum of ITO substrates covered with (SnO_2+ perovskite) films.

ITO with high transmittance was purchased from YiYang South China Xiangcheng Technology Co., Ltd, the product specification is "6 Ohm JM Etch". The ITO in the manuscript was used directly after purchase, without further processing. As shown in Figure S26(a), the transmittance of ITO substrate was measured, and we obtained that the light transmittance was 94% at 590 nm, which was consistent with the value provided by the company. The absorbance of the perovskite/SnO_2/ITO film was then measured, showing 98.8% at 550 nm, shown in Figure S26(b). The increase of transmittance comes from the decrease of reflection loss, as the refractive index of perovskite is much higher than ITO/glass. We agree with reviewer's suggestion to include the transmittance data as Fig S in SI.

Reference:

[1] Selberherr, Siegfried, *Analysis and simulation of semiconductor devices*, Springer-Verlag Wien, **1984**.

[2] A. M. A. Leguy, P. Azarhoosh, M. I. Alonso, M. Campoy-Quiles, P. R. F. Barnes, *Nanoscale* **2015**, *8*, 6317.

[3] T. Leijtens, S. D. Stranks, G. E. Eperon, R. Lindblad, E. M. J. Johansson, I. J. Mcpherson, H. K. Rensmo, J. M. Ball, M. M. Lee, H. J. Snaith, *ACS Nano* **2014**, *8*, 7147.

[4] A. Walsh, D. O. Scanlon, S. Chen, X. Gong, S. H. Wei, *Angew. Chem.* **2015**, *127*, 1811.

[5] M. Sendner, P. K. Nayak, D. A. Egger, S. Beck, C. Müller, B. Epding, W. Kowalsky, L. Kronik, H. J. Snaith, A. Pucci, *Mater. Horiz.* **2016**, *3*, 613.